

Euclid preparation

TBD. Forecast impact of super-sample covariance on 3x2pt analysis with Euclid

Euclid Collaboration: D. Sciotti^{1,2,3*}, S. Gouyou Beauchamps^{4,5,6}, V. F. Cardone^{2,3}, S. Camera^{7,8,9}, I. Tutusaus^{10,11,12,5}, F. Lacasa^{11,13}, Alexandre Barreira^{14,15}, A. Gorce¹⁶, M. Aubert^{17,18}, P. Baratta⁴, R. E. Upham¹⁹, M. Bonici²⁰, C. Carbone²⁰, S. Casas²¹, S. Ilic^{22,23,10}, M. Martinelli^{2,3}, Z. Sakr^{24,25,10}, A. Schneider²⁶, R. Maoli^{1,2}, R. Scaramella^{2,3}, S. Escoffier⁴, W. Gillard⁴, N. Aghanim¹³, A. Amara²⁷, S. Andreon²⁸, N. Auricchio²⁹, M. Baldi^{30,29,31}, S. Bardelli²⁹, D. Bonino⁹, E. Branchini^{32,33}, M. Brescia^{34,35}, J. Brinchmann³⁶, V. Capobianco⁹, J. Carretero^{37,38}, F. J. Castander^{12,5}, M. Castellano², S. Cavuoti^{35,39}, A. Cimatti⁴⁰, R. Cledassou^{23,41†}, G. Congedo⁴², C. J. Conselice¹⁹, L. Conversi^{43,44}, Y. Copin¹⁷, L. Corcione⁹, F. Courbin⁴⁵, H. M. Courtois⁴⁶, M. Cropper⁴⁷, A. Da Silva^{48,49}, H. Degaudenzi⁵⁰, J. Dinis^{49,48}, F. Dubath⁵⁰, X. Dupac⁴⁴, S. Dusini⁵¹, M. Farina⁵², S. Farrens⁵³, P. Fosalba^{12,5}, M. Frailis⁵⁴, E. Franceschi²⁹, M. Fumana²⁰, S. Galeotta⁵⁴, B. Garilli²⁰, B. Gillis⁴², C. Giocoli^{29,31}, A. Grazian⁵⁵, F. Grupp^{56,57}, L. Guzzo^{58,28,59}, S. V. H. Haugan⁶⁰, W. Holmes⁶¹, I. Hook⁶², F. Hormuth⁶³, A. Hornstrup^{64,65}, P. Hudelot⁶⁶, K. Jahnke⁶⁷, B. Joachimi⁶⁸, E. Keihänen⁶⁹, S. Kermiche⁴, A. Kiessling⁶¹, M. Kunz¹¹, H. Kurki-Suonio^{70,71}, P. B. Lilje⁶⁰, V. Lindholm^{70,71}, I. Lloro⁷², D. Maino^{58,20,59}, O. Mansutti⁵⁴, O. Marggraf⁷³, K. Markovic⁶¹, N. Martinet⁷⁴, F. Marulli^{75,29,31}, R. Massey⁷⁶, S. Maurogordato⁷⁷, E. Medinaceli²⁹, S. Mei⁷⁸, Y. Mellier^{79,66,80}, M. Meneghetti^{29,31}, G. Meylan⁴⁵, M. Moresco^{75,29}, L. Moscardini^{75,29,31}, E. Munari⁵⁴, S.-M. Niemi⁸¹, C. Padilla³⁷, S. Paltani⁵⁰, F. Pasian⁵⁴, K. Pedersen⁸², V. Pettorino⁸³, S. Pires⁵³, G. Polenta⁸⁴, M. Poncet²³, L. A. Popa⁸⁵, F. Raison⁵⁶, R. Rebolo^{86,87}, A. Renzi^{88,51}, J. Rhodes⁶¹, G. Riccio³⁵, E. Romelli⁵⁴, M. Roncarelli²⁹, R. Saglia^{89,56}, D. Sapone⁹⁰, B. Sartoris^{89,54}, M. Schirmer⁶⁷, P. Schneider⁷³, A. Secroun⁴, G. Seidel⁶⁷, S. Serrano^{5,6}, C. Sirignano^{88,51}, G. Sirri³¹, L. Stanco⁵¹, J.-L. Starck⁹¹, P. Tallada-Crespí^{92,38}, A. N. Taylor⁴², I. Tereno^{48,93}, R. Toledo-Moreo⁹⁴, F. Torradeflot^{38,92}, E. A. Valentijn⁹⁵, L. Valenziano^{29,96}, T. Vassallo^{89,54}, A. Veropalumbo²⁸, Y. Wang⁹⁷, J. Weller^{89,56}, A. Zacchei^{54,98}, G. Zamorani²⁹, J. Zoubian⁴, E. Zucca²⁹, A. Biviano^{54,98}, A. Boucaud⁷⁸, E. Bozzo⁵⁰, C. Colodro-Conde⁸⁶, D. Di Ferdinando³¹, R. Farinelli²⁹, J. Graciá-Carpio⁵⁶, N. Mauri^{40,31}, C. Neissner^{37,38}, V. Scottez^{79,99}, M. Tenti⁹⁶, Y. Akrami^{100,101,102,103,104}, V. Allevato^{35,105}, C. Baccigalupi^{106,98,54,107}, M. Ballardini^{108,109,29}, F. Bernardeau^{110,66}, A. Blanchard¹⁰, S. Borgani^{54,111,107,98}, A. S. Borlaff^{112,113}, C. Burigana^{114,96}, R. Cabanac¹⁰, A. Cappi^{29,77}, C. S. Carvalho⁹³, G. Castignani^{75,29}, T. Castro^{54,107,98}, G. Cañas-Herrera^{81,115}, K. C. Chambers¹¹⁶, A. R. Cooray¹¹⁷, J. Coupon⁵⁰, A. Díaz-Sánchez¹¹⁸, S. Davini³³, G. De Lucia⁵⁴, G. Desprez¹¹⁹, S. Di Domizio¹²⁰, J. A. Escartin Vigo⁵⁶, I. Ferrero⁶⁰, F. Finelli^{29,96}, L. Gabarra^{88,51}, K. Ganga⁷⁸, J. Garcia-Bellido¹⁰⁰, E. Gaztanaga^{12,5,27}, F. Giacomini³¹, G. Gozaliasl⁷⁰, H. Hildebrandt¹²¹, J. Jacobson¹²², J. J. E. Kajava^{123,124}, V. Kansal⁹¹, C. C. Kirkpatrick⁶⁹, L. Legrand¹¹, A. Loureiro^{125,104}, J. Macias-Perez¹²⁶, M. Magliocchetti⁵², G. Mainetti¹²⁷, C. J. A. P. Martins^{128,36}, S. Matthew⁴², L. Maurin¹³, R. B. Metcalfe⁷⁵, M. Migliaccio^{129,130}, P. Monaco^{111,54,107,98}, G. Morgante²⁹, S. Nadathur²⁷, A. A. Nucita^{131,132,133}, M. Pöntinen⁷⁰, L. Patrizii³¹, V. Popa⁸⁵, C. Porciani⁷³, D. Potter²⁶, A. Pourtsidou^{42,134}, A. G. Sánchez⁵⁶, E. Sefusatti^{54,98,107}, M. Sereno^{29,31}, P. Simon⁷³, A. Spurio Mancini⁴⁷, J. Stadel²⁶, J. Steinwagner⁵⁶, R. Teyssier¹³⁵, S. Toft^{65,136}, M. Tucci⁵⁰, C. Valieri³¹, J. Valiviita^{70,71}, M. Viel^{98,54,106,107}

(Affiliations can be found after the references)

October 25, 2023

ABSTRACT

Context. Deviations from Gaussianity in the distribution of the fields probed by large-scale structure surveys generate additional terms in the data covariance matrix, increasing the uncertainties in the measurement of the cosmological parameters. Super-sample covariance (SSC) is among the largest of these non-Gaussian contributions, with the potential to significantly degrade constraints on some of the parameters of the cosmological model under study – especially for weak lensing cosmic shear.

Aims. We compute and validate the impact of SSC on the forecast uncertainties on the cosmological parameters for the *Euclid* photometric survey, and investigate how its impact depends on the forecast specifics.

Methods. We follow the recipes outlined by the Euclid Collaboration (EC) to produce 1σ constraints through a Fisher matrix analysis, considering the Gaussian covariance alone and adding the SSC term – computed through the public code PySSC. The constraints are produced both by using *Euclid*'s photometric probes in isolation and by combining them in the '3x2pt' analysis.

Results. We meet EC requirements on the forecasts validation, with an agreement at the 10% level between the mean results of the two pipelines considered, and find the SSC impact to be non-negligible – halving the Figure of Merit of the dark energy parameters (w_0 , w_a) in the 3x2pt case

and substantially increasing the uncertainties on $\Omega_{m,0}$, w_0 , and σ_8 for the weak lensing probe. We find photometric galaxy clustering to be less affected as a consequence of the lower probe response. The relative impact of SSC does not show significant changes under variations of the redshift binning scheme, while it is smaller for weak lensing when marginalising over the multiplicative shear bias nuisance parameters, which also leads to poorer constraints on the cosmological parameters. Finally, we explore how the use of prior information on the shear and galaxy bias changes the SSC impact. It turns out that improving shear bias priors does not have a significant impact, while galaxy bias must be calibrated to sub-percent level in order to increase the Figure of Merit by the large amount needed to achieve the value when SSC is not included.

Key words. Cosmology: cosmological parameters – theory – large-scale structure of Universe – observations

1. Introduction

The last decades have witnessed a remarkable improvement in the precision of cosmological experiments, and consequently in our grasp of the general properties of the Universe. The Λ CDM concordance cosmological model provides an exquisite fit to observational data coming both from the very early and very late Universe, but, despite its success, the basic components it postulates are poorly understood. In fact, the nature of the mechanism responsible for the observed accelerated cosmic expansion (Riess et al. 1998; Perlmutter et al. 1999), dark energy, and of the component accounting for the vast majority of the matter content, dark matter, is still unknown. Upcoming Stage IV surveys like the Vera C. Rubin Observatory Legacy Survey of Space and Time (LSST, Ivezić et al. 2019), the Nancy Grace Roman Space Telescope (Spergel et al. 2015), and the *Euclid* mission (Laureijs et al. 2011) promise to help deepen our understanding of these dark components and the nature of gravity on cosmological scales, by providing unprecedented observations of the large-scale structures (LSS) of the Universe.

Because of their high accuracy and precision, these next-generation experiments will require accurate modelling of both the theory and the covariance of the observables under study to produce precise and unbiased estimates of the cosmological parameters. Amongst the different theoretical issues to deal with is the super-sample covariance (SSC), a form of sample variance arising from the finiteness of the survey area. It has been first introduced for cluster counts in Hu & Kravtsov (2003) – sometimes being referred to as ‘beat coupling’, see Rimes & Hamilton (2006); Hamilton et al. (2006) – and has received a lot of attention in recent years (Takada & Hu 2013; Li et al. 2014; Barreira et al. 2018b; Digman et al. 2019; Bayer et al. 2022; Yao et al. 2023). See also Linke et al. (2023) for an insightful discussion on SSC in real space. From here on Barreira et al. (2018b) will be cited as B18.

The effect arises from the coupling between ‘super-survey’ modes, with wavelength λ larger than the survey typical size $L = V_s^{1/3}$ (where V_s is the volume of the survey) and short-wavelength ($\lambda < L$) modes. This coupling is in turn due to the significant nonlinear evolution undergone by low-redshift cosmological probes (contrary to, for example, the cosmic microwave background), which breaks the initial homogeneity of the density field, making its growth position-dependent. In Fourier space, this means that modes with different wavenumber $k = 2\pi/\lambda$ become coupled. The modulation induced by the super-survey modes is equivalent to a change in the background density of the observed region, which affects and correlates all LSS probes. It is accounted for as an additional, non-diagonal term in the data covariance matrix beyond the Gaussian covariance, which is the only term that would exist if the random field under study was Gaussian. Being the most affected by nonlinear dynamics, the smaller scales are heavily impacted by SSC, where the effect

is expected to be the dominant source of statistical uncertainty for the 2-point statistics of weak lensing cosmic shear (WL): it has in fact been found to increase unmarginalised uncertainties up to a factor of about 2 (for a *Euclid*-like survey, see Barreira et al. 2018a; Gouyou Beauchamps et al. 2022). In the case of photometric galaxy clustering (GCph; again, for a *Euclid*-like survey), Lacasa & Grain (2019) – hereafter LG19 – found the cumulative signal-to-noise to be decreased by a factor around 6 at $\ell_{\max} = 2000$. These works, however, either do not take into account marginalised uncertainties or the variability of the probe responses, do not include cross-correlations between probes, or do not follow the full specifics of the *Euclid* survey detailed below.

The present article has two aims. First, we intend to validate the forecast constraints on the cosmological parameters both including and neglecting the SSC term; these are produced using two independent codes, whose only shared feature is their use of the public Python module PySSC¹² (LG19) to compute the fundamental elements needed to build the SSC matrix. Second, we investigate the impact of SSC on the marginalised uncertainties and the dark energy Figure of Merit (FoM), both obtained through a Fisher forecast of the constraining power of *Euclid*’s photometric observables.

The article is organized as follows: Sect. 2 presents an overview of the SSC and the approximations used to compute it. In Sect. 3 we outline the theoretical model and specifics used to produce the forecasts, while Sect. 4 provides technical details on the codes’ implementation and validation. Then, we study in Sect. 5 the impact of SSC on *Euclid* constraints, for different binning schemes and choices of systematic errors and priors. Finally, we present our conclusions in Sect. 6.

2. SSC theory and approximations

2.1. General formalism

Throughout the article, we will work with 2D-projected observables, namely the angular Power Spectrum (PS), which in the Limber approximation (Limber 1953; Kaiser 1998) can be expressed as

$$C_{ij}^{AB}(\ell) = \int dV W_i^A(z) W_j^B(z) P_{AB}(k_\ell, z), \quad (1)$$

giving the correlation between probes A and B in the redshift bins i and j , as a function of the multipole ℓ ; $k_\ell = (\ell+1/2)/r(z)$ is the Limber wavenumber and $W_i^A(z)$, $W_j^B(z)$ are the survey weight functions (WFs), or “kernels”. Here we consider as the element of integration $dV = r^2(z) \frac{dz}{c}$ which is the comoving volume element per steradian, with $r(z)$ being the comoving distance.

The SSC between two projected observables arises because real observations of the Universe are always limited by a survey window function $\mathcal{M}(\mathbf{x})$. Taking $\mathcal{M}(\mathbf{x})$ at a given redshift, thus

* e-mail: davide.sciotti@uniroma1.it

† Deceased

¹<https://github.com/fabienlacasa/PySSC>

²<https://pyssc.readthedocs.io/en/latest/index.html>

considering only its angular dependence $\mathcal{M}(\hat{\mathbf{n}})^3$, with $\hat{\mathbf{n}}$ the unit vector on a sphere, we can define the background density contrast as (Lacasa et al. 2018)

$$\delta_b(z) = \frac{1}{\Omega_S} \int d^2\hat{\mathbf{n}} \mathcal{M}(\hat{\mathbf{n}}) \delta_m[r(z)\hat{\mathbf{n}}, z], \quad (2)$$

with $r(z)\hat{\mathbf{n}} = \mathbf{x}$. In this equation, $\delta_m(\mathbf{x}, z) = [\rho_m(\mathbf{x}, z)/\bar{\rho}_m(z) - 1]$ is the matter density contrast, with $\rho_m(\mathbf{x}, z)$ the matter density and $\bar{\rho}_m(z)$ its spatial average over the whole Universe at lookback time z and Ω_S the solid angle observed by the survey.

In other words, δ_b is the spatial average of the density contrast $\delta_m(\mathbf{x}, z)$ over the survey area:

$$\langle \delta_m(\mathbf{x}, z) \rangle_{\text{universe}} = 0, \quad (3)$$

$$\langle \delta_m(\mathbf{x}, z) \rangle_{\text{survey}} = \delta_b(z). \quad (4)$$

The covariance of this background density contrast is defined as $\sigma^2(z_1, z_2) \equiv \langle \delta_b(z_1) \delta_b(z_2) \rangle$ and in the full-sky approximation is given by (Lacasa & Rosenfeld 2016)

$$\sigma^2(z_1, z_2) = \frac{1}{2\pi^2} \int dk k^2 P_{\text{mm}}^{\text{lin}}(k, z_{12}) j_0(kr_1) j_0(kr_2), \quad (5)$$

with $P_{\text{mm}}^{\text{lin}}(k, z_{12}) \equiv D(z_1)D(z_2)P_{\text{mm}}^{\text{lin}}(k, z = 0)$ the linear matter cross-spectrum between z_1 and z_2 , $D(z)$ the linear growth factor and $j_0(kr_i)$ the first-order spherical Bessel function, and $r_i = r(z_i)$. The use of the linear PS reflects the fact that the SSC is caused by long-wavelength perturbations, which are well described by linear theory. Note that we have absorbed the Ω_S^{-1} prefactor of Eq. (2), equal to 4π in full sky, in the dV_i terms, being them the comoving volume element per steradian.

Depending on the portion of the Universe observed, δ_b will be different, and in turn the PS of the considered observables $P_{AB}(k_\ell, z)$ (appearing in Eq. 1) will react to this change in the background density through the *probe response* $\partial P_{AB}(k_\ell, z)/\partial \delta_b$.

SSC is then the combination of these two elements, encapsulating the covariance of δ_b and the response of the observables to a change in δ_b ; the general expression of the SSC between two projected observables is (Lacasa & Rosenfeld 2016):

$$\text{Cov}_{\text{SSC}} [C_{ij}^{AB}(\ell), C_{kl}^{CD}(\ell')] = \int dV_1 dV_2 W_i^A(z_1) W_j^B(z_1) \times W_k^C(z_2) W_l^D(z_2) \frac{\partial P_{AB}(k_\ell, z_1)}{\partial \delta_b} \frac{\partial P_{CD}(k_{\ell'}, z_2)}{\partial \delta_b} \sigma^2(z_1, z_2). \quad (6)$$

We adopt the approximation presented in Lacasa & Grain (2019), which assumes the responses to vary slowly in redshift with respect to $\sigma^2(z_1, z_2)$. We can then approximate the responses with their weighted average over the $W_i^A(z)$ kernels (Gouyou Beauchamps et al. 2022):

$$\frac{\partial \bar{P}_{AB}(k_\ell, z)}{\partial \delta_b} = \frac{\int dV W_i^A(z) W_j^B(z) \partial P_{AB}(k_\ell, z)/\partial \delta_b}{\int dV W_i^A(z) W_j^B(z)}, \quad (7)$$

and pull them out of the integral. The denominator on the right-hand side (r.h.s.) acts as a normalization term, which we call I_{ij}^{AB} . We can further manipulate the above expression by factorising the probe response as

$$\frac{\partial P_{AB}(k_\ell, z)}{\partial \delta_b} = R^{AB}(k_\ell, z) P_{AB}(k_\ell, z), \quad (8)$$

³Here we do not consider a redshift dependence of $\mathcal{M}(\hat{\mathbf{n}})$ but this can happen for surveys with significant depth variations across the sky. This is discussed in Lacasa et al. (2018).

where $R^{AB}(k_\ell, z)$, the *response coefficient*, can be obtained from simulations, as in Wagner et al. (2015a,b); Li et al. (2016); Barreira et al. (2019), or from theory (e.g. via the halo model) as in Takada & Hu (2013); Krause & Eifler (2017); Rizzato et al. (2019). Following LG19, we can introduce the probe response of the angular power spectrum $C_{ij}^{AB}(\ell)$ in a similar way, using Eq. (1)

$$\frac{\partial C_{ij}^{AB}(\ell)}{\partial \delta_b} = \int dV W_i^A(z) W_j^B(z) \frac{\partial P_{AB}(k_\ell, z)}{\partial \delta_b} \equiv R_{ij}^{AB}(\ell) C_{ij}^{AB}(\ell). \quad (9)$$

Substituting Eq. (8) into the r.h.s. of Eq. (7), using Eq. (9) and dividing by the sky fraction observed by the telescope $f_{\text{sky}} = \Omega_S/4\pi$, we get the expression of the SSC which will be used throughout this work:

$$\text{Cov}_{\text{SSC}} [C_{ij}^{AB}(\ell) C_{kl}^{CD}(\ell')] \simeq f_{\text{sky}}^{-1} [R_{ij}^{AB}(\ell) C_{ij}^{AB}(\ell) \times R_{kl}^{CD}(\ell') C_{kl}^{CD}(\ell') S_{i,j,k,l}^{A,B,C,D}]. \quad (10)$$

In the above equation, we have defined

$$S_{i,j,k,l}^{A,B,C,D} \equiv \int dV_1 dV_2 \frac{W_i^A(z_1) W_j^B(z_1)}{I_{ij}^{AB}} \frac{W_k^C(z_2) W_l^D(z_2)}{I_{kl}^{CD}} \sigma^2(z_1, z_2). \quad (11)$$

The $S_{i,j,k,l}^{A,B,C,D}$ matrix (referred to as S_{ijkl} from here on) is the volume average of $\sigma^2(z_1, z_2)$, and is a dimensionless quantity. It is computed through the public Python module PySSC, released alongside the above-mentioned LG19. A description of the way this code has been used, and some comments on the inputs to provide and the outputs it produces, can be found in Sect. 4.

The validity of Eq. (10) has been tested in LG19 in the case of GCph and found to reproduce the Fisher matrix (FM, Tegmark et al. 1997) elements and signal-to-noise ratio from the original expression (Eq. 6):

- within 10% discrepancy up to $\ell \simeq 1000$ for $R_{ij}^{AB}(k_\ell, z) = \text{const}$;
- within 5% discrepancy up to $\ell \simeq 2000$ when using the linear approximation in scale for $R^{AB}(k_\ell, z)$ provided in Appendix C of the same work.

The necessity to push the analysis to smaller scales, as well as to investigate the SSC impact not only for GCph but also for WL and their cross-correlation, has motivated a more exhaustive characterization of the probe response functions, which will be detailed in the next section.

Another approximation used in the literature has been presented in (Krause & Eifler 2017): the $\sigma^2(z_1, z_2)$ term is considered as a Dirac delta in $z_1 = z_2$. This greatly simplifies the computation, because the double redshift integral $dV_1 dV_2$ collapses to a single one. This approximation is used by the other two available public codes which can compute the SSC: PyCCL (Chisari et al. 2019) and CosmoLike (Krause & Eifler 2017). Lacasa et al. (2018) compared this approximation against the one used in this work, finding the former to fare better for wide redshift bins (as in the case of WL), and the latter for narrow bins (as in the case of GCph).

Lastly, we note that in Eq. (10) we account for the sky coverage of the survey through the full-sky approximation by simply dividing by f_{sky} ; in the case of *Euclid* we have $\Omega_S = 14\,700 \text{ deg}^2 \simeq 4.4776 \text{ sr}$. The validity of this approximation has

been discussed in Gouyou Beauchamps et al. (2022), and found to agree at the percent level on the marginalized parameter constraints with the more rigorous treatment accounting for the exact survey geometry, when considering large survey areas. For this test they considered an area of 15 000 deg² and a survey geometry very close to what *Euclid* will have, i.e. the full-sky with the ecliptic and galactic plane removed. Intuitively, the severity of the SSC decays as f_{sky}^{-1} because larger survey volumes are able to accommodate more Fourier modes.

Note that we are considering here the maximum sky coverage that *Euclid* will reach, i.e. the final data release (DR3). For the first data release (DR1), the sky coverage will be significantly lower and the full-sky approximation will not hold. In that case, the partial-sky recipe proposed in Gouyou Beauchamps et al. (2022) should be considered instead.

2.2. Probe response

As mentioned in the previous section, one of the key ingredients of the SSC is the probe response. To compute this term for the probes of interest, we build upon previous works (Wagner et al. 2015a,b; Li et al. 2016; Barreira & Schmidt 2017, B18), and compute the response coefficient of the matter PS as

$$R^{\text{mm}}(k, z) = \frac{\partial \ln P_{\text{mm}}(k, z)}{\partial \delta_{\text{b}}} = 1 - \frac{1}{3} \frac{\partial \ln P_{\text{mm}}(k, z)}{\partial \ln k} + G_1^{\text{mm}}(k, z). \quad (12)$$

$G_1^{\text{mm}}(k, z)$ is called the *growth-only response*; it is constant and equal to 26/21 in the linear regime and it can be computed in the nonlinear regime using separate universe simulations, as done in Wagner et al. (2015b), whose results have been used in B18 (and in the present work). The latter uses a power law to extrapolate the values of the response for $k > k_{\text{max}}$, with k_{max} being the maximum wavenumber at which the power spectrum is reliably measured from the simulations. Further details on this extrapolation, as well as on the redshift and scale dependence of R^{mm} , can be found respectively in Sect. 2 and in the left panel of Fig. 1 of B18. We note that R^{mm} is the response coefficient of isotropic large-scale *density* perturbations; we neglect the contribution from the anisotropic *tidal-field* perturbations to the total response of the power spectrum (and consequently to the SSC), which has been shown in B18 to be subdominant for WL with respect to the first contribution (about 5% of the total covariance matrix at $\ell \gtrsim 300$).

The probes considered in the present study are WL, GCph and their cross-correlation (XC); the corresponding power spectra are given by the following expressions

$$P_{AB}(k, z) = \begin{cases} P_{\text{mm}}(k, z) & A = B = \text{L} \\ b_{(1)}(z)P_{\text{mm}}(k, z) & A = \text{L}, B = \text{G} \\ b_{(1)}^2(z)P_{\text{mm}}(k, z) & A = B = \text{G}, \end{cases} \quad (13)$$

with (L, G) for (shear, position), $P_{\text{mm}}(k, z)$ the *nonlinear* matter PS and $b_{(1)}(z)$ the linear, scale-independent and deterministic galaxy bias. A comment is in order about the way we model the galaxy-matter and galaxy-galaxy power spectra. We are indeed using a linear bias, but the nonlinear recipe for the matter power spectrum $P_{\text{mm}}(k, z)$. This is reminiscent of the hybrid 1-loop perturbation theory (PT) model adopted by, e.g., the DES Collaboration in the analysis of the latest data release (Krause et al. 2021; Pandey et al. 2022), but we drop the higher-order

bias terms. This simplified model has been chosen in order to be consistent with the IST:F (Euclid Collaboration: Blanchard et al. 2020, from hereon EC20) forecasts, against which we compare our results (in the Gaussian case) to validate them. We are well aware that scale cuts should be performed in order to avoid biasing the constraints, but we are here more interested in the relative impact of SSC on the constraints than the constraints themselves. Any systematic error due to the approximate modelling should roughly cancel out in the ratio we will compute later on. Note also that we choose to include a perfectly Poissonian shot noise term in the covariance matrix, rather than in the signal, as can be seen in Eq. (25). The responses for the different probes can be obtained in terms⁴ of $R^{\text{mm}}(k, z)$ by using the relations between matter and galaxy PS given above

$$R^{\text{gg}}(k, z) = \frac{\partial \ln P_{\text{gg}}(k, z)}{\partial \delta_{\text{b}}} = R^{\text{mm}}(k, z) + 2b_{(1)}^{-1}(z) \left[b_{(2)}(z) - b_{(1)}^2(z) \right], \quad (14)$$

and similarly for R^{gm} :

$$R^{\text{gm}}(k, z) = \frac{\partial \ln P_{\text{gm}}(k, z)}{\partial \delta_{\text{b}}} = R^{\text{mm}}(k, z) + b_{(1)}^{-1}(z) \left[b_{(2)}(z) - b_{(1)}^2(z) \right]. \quad (15)$$

Having used the definitions of the first and second-order galaxy bias, i.e., $b_{(1)}(z) = (\partial n_{\text{g}} / \partial \delta_{\text{b}}) / n_{\text{g}}$ and $b_{(2)}(z) = (\partial^2 n_{\text{g}} / \partial \delta_{\text{b}}^2) / n_{\text{g}}$, with n_{g} the total angular galaxy number density, in arcmin⁻². In the following, where there is no risk of ambiguity, we will drop the subscript in parenthesis when referring to the first-order galaxy bias – i.e., $b(z) = b_{(1)}(z)$ – to shorten the notation, and we will indicate the value of the first-order galaxy bias in the i -th redshift bin with $b_i(z)$. More details on the computation of these terms can be found in Sect. 3.6. Note that Eqs. (14)–(15) are obtained by differentiating a PS model for a galaxy density contrast defined with respect to (w.r.t.) the *observed* galaxy number density, and so they already account for the fact that the latter also “responds” to the large scale perturbation δ_{b} . This is also the reason why $R_{ij}^{\text{GG}}(\ell)$ can have negative values: for galaxy clustering, the (number) density contrast δ_{gal} is measured w.r.t. the observed, local number density \bar{n}_{gal} : $\delta_{\text{gal}} = n_{\text{gal}} / \bar{n}_{\text{gal}} - 1$. The latter also responds to a background density perturbation δ_{b} , and it can indeed happen that \bar{n}_{gal} grows with δ_{b} faster than n_{gal} , which leads to δ_{gal} decreasing with increasing δ_{b} (which also implies $\partial C_{ij}^{\text{GG}}(\ell) / \partial \delta_{\text{b}} < 0$). We also stress the fact that the second-order galaxy bias appearing in the galaxy-galaxy and galaxy-lensing response coefficients is not included in the signal, following EC20. Once computed in this way, the response coefficient can be projected in harmonic space using Eq. (9), and inserted in Eq. (10) to compute the SSC in the LG19 approximation. The projected $R_{ij}^{\text{AB}}(\ell)$ functions are shown in Fig. 1.

3. Forecasts specifics

In order to forecast the uncertainties in the measurement of the cosmological parameters, we will follow the prescriptions of the *Euclid* forecast validation study (EC20), with some updates to the most recent results from the EC, which are used for the third Science Performance Verification (SPV) of *Euclid* before

⁴Since we are using the nonlinear matter power spectrum $P_{\text{mm}}(k, z)$, we do not force $R^{\text{mm}}(k, z)$ to reduce to its linear expression, that is to say, we do not set $G_1^{\text{mm}} = 26/21$ in Eq. (12).

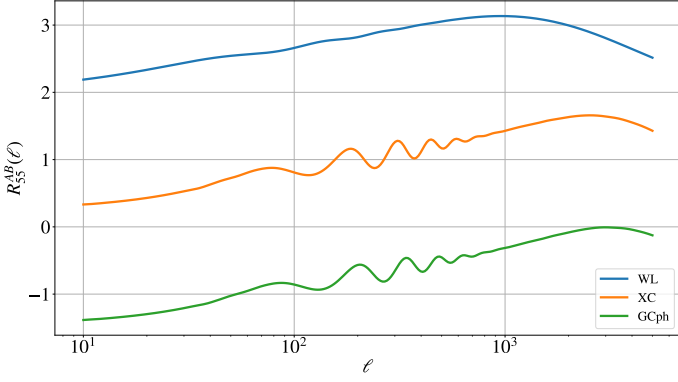


Fig. 1. Projected response coefficients for the WL and GCph probes and their cross-correlation, for the central redshift bin ($0.8 \lesssim z \lesssim 0.9$) – the shape and amplitude of the functions for different redshift pairs are analogous. For WL, the baryon acoustic oscillations wiggles are smoothed out by the projection, due to the kernels being larger than the GCph ones. The different amplitude of the response is one of the main factors governing the severity of SSC.

launch. In particular, the update concerns the fiducial value of the linear bias, the redshift distribution $n(z)$ and the multipole binning.

Once again, the observable under study is the angular PS of probe A in redshift bin i and probe B in redshift bin j , given in the Limber approximation by Eq. (1). The $P_{AB}(k_\ell, z)$ multi-probe power spectra are given in Eq. (13); in the following, we will refer interchangeably to the probes (WL, XC, GCph) and their auto- and cross-spectra (respectively, LL, GL, GG).

3.1. Redshift distribution

First, we assume that the same galaxy population is used to probe both the WL and the GCph PS. We therefore set

$$n_i^L(z) = n_i^G(z) = n_i(z), \quad (16)$$

where $n_i^L(z)$ and $n_i^G(z)$ are respectively the distribution of sources and lenses in the i -th redshift bin. Then, the same equality applies for the total source and lens number density, \bar{n}^L and \bar{n}^G .

A more realistic galaxy redshift distribution than the analytical one presented in EC20 can be obtained from simulations. We use the results from *Euclid* Collaboration: Pocino et al. (2021), in which the $n(z)$ is constructed from photometric redshift estimates in a 400 deg² patch of the Flagship 1 simulation (Potter et al. 2017), using the training-based directional neighbourhood fitting algorithm (DNF, De Vicente et al. 2016).

The training set is a random subsample of objects with true (spectroscopic) redshifts known from the Flagship simulation. We choose the fiducial case presented in *Euclid* Collaboration: Pocino et al. (2021), which takes into account a drop in completeness of the spectroscopic training sample with increasing magnitude. A cut in magnitude $I_E < 24.5$, isotropic and equal for all photometric bands, is applied, corresponding to the optimistic *Euclid* setting. The DNF algorithm then produces a first estimate of the photo- z , z_{mean} , using as metric the objects' closeness in colour and magnitude space to the training samples. A second estimate of the redshift, z_{mc} , is computed from a Monte Carlo draw from the nearest neighbour in the DNF metric. The final distributions for the different redshift bins, $n_i(z)$, are obtained by assigning the sources to the respective bins using their z_{mean} , and then taking the histogram of the z_{mc} values in each of

the bins – following what has been done in real surveys such as the Dark Energy Survey (Crocco et al. 2019; Hoyle et al. 2018).

As a reference setting, we choose to bin the galaxy distribution into $\mathcal{N}_b = 10$ equipopulated redshift bins, with edges

$$z_{\text{edges}} = \{0.001, 0.301, 0.471, 0.608, 0.731, 0.851, 0.980, 1.131, 1.335, 1.667, 2.501\}. \quad (17)$$

The total galaxy number density is $\bar{n} = 28.73 \text{ arcmin}^{-2}$. As a comparison, this was set to 30 arcmin^{-2} in EC20. Note that this choice of redshift binning will be discussed and varied in Sect. 5.4.

3.2. Weight functions

We model the radial kernels, or weight functions, for WL and GCph following once again EC20. Adopting the eNLA (extended nonlinear alignment) prescription for modelling the intrinsic alignment (IA) contribution, the weight function $\mathcal{W}_i^A(z)$ for the lensing part is given by (see e.g. Kitching et al. 2017; Kilbinger et al. 2017; Taylor et al. 2018)

$$\mathcal{W}_i^L(z) = \mathcal{W}_i^G(z) - \frac{\mathcal{A}_{\text{IA}} C_{\text{IA}} \Omega_{\text{m},0} \mathcal{F}_{\text{IA}}(z)}{D(z)} \mathcal{W}_i^{\text{IA}}(z), \quad (18)$$

where we have defined⁵

$$\mathcal{W}_i^G(z) = \frac{3}{2} \left(\frac{H_0}{c} \right)^2 \Omega_{\text{m},0} (1+z) r(z) \int_z^{z_{\text{max}}} \frac{n_i(z')}{\bar{n}} \left[1 - \frac{r(z)}{r(z')} \right] dz', \quad (19)$$

and

$$\mathcal{W}_i^{\text{IA}}(z) = \frac{1}{c} \frac{n_i(z)}{\bar{n}} H(z). \quad (20)$$

Finally, in Eq. (18), \mathcal{A}_{IA} is the overall IA amplitude, C_{IA} a constant, $\mathcal{F}_{\text{IA}}(z)$ a function modulating the dependence on redshift, and $D(z)$ is the linear growth factor. More details on the IA modelling are given in Sect. 3.5.

The GCph weight function is equal to the IA one, as long as Eq. (16) holds:

$$\mathcal{W}_i^G(z) = \mathcal{W}_i^{\text{IA}}(z) = \frac{1}{c} \frac{n_i(z)}{\bar{n}} H(z). \quad (21)$$

Fig. 2 shows the redshift dependence of Eqs. (18) and (21), for all redshift bins. Note that we choose to include the galaxy bias term $b_i(z)$ in the PS (see Eq. 13) rather than in the galaxy kernel, as opposed to what has been done in EC20. This is done to compute the galaxy response as described in Sect. 2.2. Since the galaxy bias is assumed constant in each bin, however, the question is of no practical relevance when computing the S_{ijkl} matrix, since the constant bias cancels out.

We note that the above definitions of the lensing and galaxy kernels ($\mathcal{W}_i^A(z)$, $A = L, G$) differ from the ones used in LG19. This is simply because of a different definition of the $C_{ij}^{AB}(\ell)$ Limber integral, which is performed in dV in LG19 and in dz in EC20. The mapping between the two conventions is simply given by the expression for the volume element:

$$dV = r^2(z) \frac{dr}{dz} dz = c \frac{r^2(z)}{H(z)} dz, \quad (22)$$

⁵Equation (19) assumes the Universe is spatially flat. For the general case, one must replace the term in brackets with $f_K(r' - r)/f_K(r')$, with $f_K(r)$ the function giving the comoving angular-diameter distance in a non-flat universe.

and

$$W_i^A(z) = \mathcal{W}_i^A(z)/r^2(z), \quad (23)$$

with $A = L, G$. In Fig. 2 we plot the values of $\mathcal{W}_i^A(z)$ to facilitate the comparison with EC20. As outlined in Appendix A, when computing the S_{ijkl} matrix through PySSC, the user can either pass the kernels in the form used in LG19 or the one used in EC20 – specifying a non-default convention parameter.

3.3. Gaussian covariance

The Gaussian part of the covariance is given by the following expression

$$\begin{aligned} \text{Cov}_G [\hat{C}_{ij}^{AB}(\ell), \hat{C}_{kl}^{CD}(\ell')] &= [(2\ell + 1) f_{\text{sky}} \Delta\ell]^{-1} \delta_{\ell\ell'}^K \\ &\times \left\{ [C_{ik}^{AC}(\ell) + N_{ik}^{AC}(\ell)] [C_{jl}^{BD}(\ell') + N_{jl}^{BD}(\ell')] \right. \\ &\left. + [C_{il}^{AD}(\ell) + N_{il}^{AD}(\ell)] [C_{jk}^{BC}(\ell') + N_{jk}^{BC}(\ell')] \right\}, \quad (24) \end{aligned}$$

where we use a hat to distinguish the estimators from the true spectra. The noise PS $N_{ij}^{AB}(\ell)$ are, for the different probe combinations

$$N_{ij}^{AB}(\ell) = \begin{cases} (\sigma_\epsilon^2/\bar{n}_i^L) \delta_{ij}^K & A = B = L \text{ (WL)} \\ 0 & A \neq B \\ (1/\bar{n}_i^G) \delta_{ij}^K & A = B = G \text{ (GCph)}. \end{cases} \quad (25)$$

In the above equations δ_{ij}^K is the Kronecker delta and σ_ϵ^2 the variance of the total intrinsic ellipticity dispersion of WL sources – where $\sigma_\epsilon = \sqrt{2}\sigma_\epsilon^{(i)}$, $\sigma_\epsilon^{(i)}$ being the ellipticity dispersion per component of the galaxy ellipse. We note that the average densities used in Eq. (25) are not the total number densities, but rather those in the i -th redshift bin. In the case of N_b equipopulated redshift bins, they can be simply written as $\bar{n}_i^A = \bar{n}^A/N_b$ for both $A = (L, G)$. Finally, we recall that f_{sky} is the fraction of the total sky area covered by the survey, while $\Delta\ell$ is the width of the multipole bin centered on a given ℓ . From Sect. 3.1 we have that $\bar{n} = 28.73 \text{ arcmin}^{-2}$, while we set $\sigma_\epsilon = 0.37$ (from the value $\sigma_\epsilon^{(i)} = 0.26$ reported in Euclid Collaboration: Martinet et al. 2019) and $f_{\text{sky}} = 0.356$ (corresponding to $\Omega_S = 14\,700 \text{ deg}^2$). We have now all the relevant formulae for the estimate of the Gaussian and the SSC terms of the covariance matrix. To ease the computation of Eq. (24) we have prepared an optimized Python module, `Spaceborne_covg`⁶, available as a public repository.

In the context of the present work, we do not consider the other non-Gaussian contribution to the total covariance matrix, the so-called connected non-Gaussian (cNG) term. This additional non-Gaussian term has been shown to be sub-dominant with respect to the Gaussian and SSC terms for WL both in Barreira et al. (2018a) and in Upham et al. (2022). For what concerns galaxy clustering, Wadekar et al. (2020) showed that the cNG term was subdominant, but this was for a spectroscopic sample so (i) they had a much larger contribution from shot-noise-related terms compared to what is considered here for the *Euclid* photometric sample, and (ii) they considered larger and more linear scales than in the present study. Lacasa (2020) showed that the cNG term in the covariance matrix of GCph only impacts

the spectral index n_s and HOD parameters, but there are a few differences between that analysis and the present work, such as the modelling of galaxy bias. Thus it is still unclear whether the cNG term has a strong impact on cosmological constraints obtained with GCph. Quantifying the impact of this term for the 3×2pt analysis with *Euclid* settings is left for future work.

3.4. Cosmological model and matter power spectrum

We adopt a flat w_0w_a CDM model, i.e., we model the dark energy equation of state with a Chevallier–Polarski–Linder (CPL) parametrisation (Chevallier & Polarski 2001; Linder 2005)

$$w(z) = w_0 + w_a z/(1+z). \quad (26)$$

We also include a contribution from massive neutrinos with total mass equal to the minimum allowed by oscillation experiments (Esteban et al. 2020) $\sum m_\nu = 0.06 \text{ eV}$, which we do not vary in the FM analysis. The vector of cosmological parameters is then

$$\theta_{\text{cosmo}} = \{\Omega_{m,0}, \Omega_{b,0}, w_0, w_a, h, n_s, \sigma_8\}, \quad (27)$$

with $\Omega_{m,0}$ and $\Omega_{b,0}$ being respectively the reduced density of total and baryonic matter today, h is the dimensionless Hubble parameter defined as $H_0 = 100 h \text{ km s}^{-1} \text{ Mpc}^{-1}$ where H_0 is the value of the Hubble parameter today, n_s the spectral index of the primordial power spectrum and σ_8 the root mean square of the linear matter density field smoothed with a sphere of radius $8 h^{-1} \text{ Mpc}$. Their fiducial values are

$$\theta_{\text{cosmo}}^{\text{fid}} = \{0.32, 0.05, -1.0, 0.0, 0.67, 0.96, 0.816\}. \quad (28)$$

This is used as input for the evaluation of the fiducial nonlinear matter PS, which is obtained using the TakaBird recipe, i.e., the HaLoFit version updated by Takahashi et al. (2012) with the Bird et al. (2012) correction for massive neutrinos. This recipe is implemented in both CLASS⁷ (Blas et al. 2011) and CAMB⁸ (Lewis et al. 2000).

3.5. Intrinsic alignment model

We use the eNLA model as in EC20, setting $C_{\text{IA}} = 0.0134$ and

$$\mathcal{F}_{\text{IA}}(z) = (1+z)^{\eta_{\text{IA}}} [\langle L \rangle(z)/L_\star(z)]^{\beta_{\text{IA}}}, \quad (29)$$

where $\langle L \rangle(z)/L_\star(z)$ is the redshift-dependent ratio of the mean luminosity over the characteristic luminosity of WL sources as estimated from an average luminosity function (see e.g. Joachimi et al. 2015, and references therein). The IA nuisance parameters vector is

$$\theta_{\text{IA}} = \{\mathcal{A}_{\text{IA}}, \eta_{\text{IA}}, \beta_{\text{IA}}\}, \quad (30)$$

with fiducial values

$$\theta_{\text{IA}}^{\text{fid}} = \{1.72, -0.41, 2.17\}. \quad (31)$$

All of the IA parameters, except for C_{IA} , will be varied in the analysis.

⁶https://github.com/davidesciotti/Spaceborne_covg

⁷https://lesgourg.github.io/class_public/class.html

⁸<https://camb.info/>

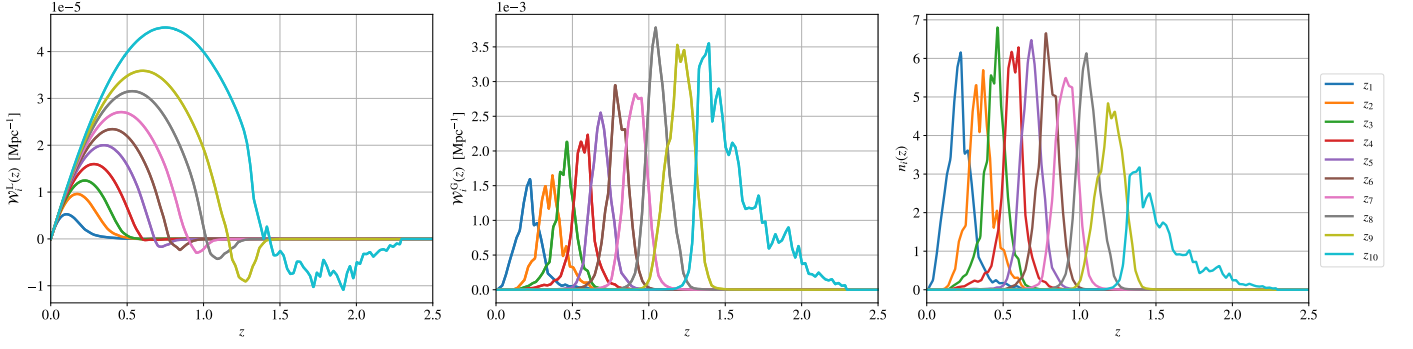


Fig. 2. First two plots: weight functions, or kernels, for the two photometric probes. The analytic expressions for these are, respectively, Eq. (18) (left, WL) and Eq. (21) (right, GCph). At high redshifts the IA term dominates over the shear term in the lensing kernels, making them negative. The rightmost plot shows the sources (and lenses) redshift distribution per redshift bin, obtained from the Flagship 1 simulation as described in Sect. 3.1

3.6. Linear galaxy bias and multiplicative shear bias

Following EC20 we model the galaxy bias as scale-independent. We move beyond the simple analytical prescription of EC20 and use the fitting function presented in *Euclid Collaboration: Pociño et al. (2021)*, obtained from direct measurements from the *Euclid* Flagship galaxy catalogue, based in turn on the Flagship 1 simulation:

$$b(z) = \frac{Az^B}{1+z} + C, \quad (32)$$

setting $(A, B, C) = (0.81, 2.80, 1.02)$.

The galaxy bias is modelled to be constant in each bin with the fiducial value obtained by evaluating Eq. (32) at effective values z_i^{eff} computed as the median of the redshift distribution considering only the part of the distribution at least larger than 10% of its maximum. The z_i^{eff} values obtained in this way are

$$z^{\text{eff}} = \{0.233, 0.373, 0.455, 0.571, 0.686, 0.796, 0.913, 1.070, 1.195, 1.628\}. \quad (33)$$

We therefore have \mathcal{N}_b additional nuisance parameters

$$\theta_{\text{gal. bias}} = \{b_1, b_2, \dots, b_{\mathcal{N}_b}\}, \quad (34)$$

with fiducial values

$$\theta_{\text{gal. bias}}^{\text{fid}} = \{1.031, 1.057, 1.081, 1.128, 1.187, 1.258, 1.348, 1.493, 1.628, 2.227\}. \quad (35)$$

We can take a further step forward towards the real data analysis by including the multiplicative shear bias parameters, m , defined as the multiplicative coefficient of the linear bias expansion of the shear field γ , see e.g. (Cragg et al. 2023):

$$\hat{\gamma} = (1 + m)\gamma + c \quad (36)$$

with $\hat{\gamma}$ the measured shear field, γ the true one, m the multiplicative and c the additive shear bias parameters (we will not consider the latter in the present analysis). The multiplicative shear bias can come from astrophysical or instrumental systematics (such as the effect of the point spread function – PSF), which affect the measurement of galaxy shapes. We take the m_i parameters (one for each redshift bin) as constant and with a fiducial

value of 0 in all bins. To include this further nuisance parameter, one just has to update the different angular PS as

$$\begin{cases} C_{ij}^{\text{LL}}(\ell) \rightarrow (1 + m_i)(1 + m_j)C_{ij}^{\text{LL}}(\ell) \\ C_{ij}^{\text{GL}}(\ell) \rightarrow (1 + m_j)C_{ij}^{\text{GL}}(\ell) \\ C_{ij}^{\text{GG}}(\ell) \rightarrow C_{ij}^{\text{GG}}(\ell), \end{cases} \quad (37)$$

where m_i is the i -th bin multiplicative bias, and the GCph spectrum is unchanged since it does not include any shear term. We will then have:

$$\theta_{\text{shear bias}} = \{m_1, m_2, \dots, m_{\mathcal{N}_b}\}, \quad (38)$$

with fiducial values

$$\theta_{\text{shear bias}}^{\text{fid}} = \{0, 0, \dots, 0\}. \quad (39)$$

These nuisance parameters – except the multiplicative shear bias ones, unless specified – are varied in the Fisher analysis so that the final parameters vector is

$$\theta = \theta_{\text{cosmo}} \cup \theta_{\text{IA}} \cup \theta_{\text{gal. bias}} \cup \theta_{\text{shear bias}},$$

and

$$\theta^{\text{fid}} = \theta_{\text{cosmo}}^{\text{fid}} \cup \theta_{\text{IA}}^{\text{fid}} \cup \theta_{\text{gal. bias}}^{\text{fid}} \cup \theta_{\text{shear bias}}^{\text{fid}},$$

both composed of $\mathcal{N}_p = 7 + 3 + 2\mathcal{N}_b = 2\mathcal{N}_b + 10$ elements.

3.6.1. Higher-order bias

In order to compute the galaxy-galaxy and galaxy-galaxy lensing probe response terms (Eqs. 14 and 15) we need the second-order galaxy bias $b_{(2)}(z)$. To do this we follow Appendix C of LG19, in which this is estimated following the halo model⁹ as (Voivodic & Barreira 2021; Barreira et al. 2021)

$$b_{(i)}(z) = \int dM \Phi_{\text{MF}}(M, z) b_{(i)}^h(M, z) \langle N|M \rangle / n_{\text{gal}}(z), \quad (40)$$

with

$$n_{\text{gal}}(z) = \int dM \Phi_{\text{MF}}(M, z) \langle N|M \rangle, \quad (41)$$

⁹We neglect here the response of $\langle N|M \rangle$ to a perturbation δ_b in the background density.

the galaxy number density, $\Phi_{\text{MF}}(M, z)$ the halo mass function (HMF), $b_{(i)}^h(M, z)$ the i -th order *halo* bias, and $\langle N|M \rangle$ the average number of galaxies hosted by a halo of mass M at redshift z (given by the halo occupation distribution, HOD). These are integrated over the mass range $\log M \in [9, 16]$, with the mass expressed in units of solar masses. The expression for the i -th order galaxy bias (Eq. 40) is the same as Eq. (C.2) of LG19, but here we are neglecting the scale dependence of the bias evaluating it at $k = 0$ so that $u(k|M=0, z) = 1$, $u(k|M, z)$ being the Fourier Transform of the halo profile. Strictly speaking, this gives us the large-scale bias, but it is easy to check that the dependence on k is negligible over the range of interest.

Although Eq. (40) allows the computation of both the first and second-order galaxy bias, we prefer to use the values of $b_{(1)}(z)$ measured from the Flagship simulation for the selected galaxy sample; this is to maintain consistency with the choices presented at the beginning Sect. 3.6. For each redshift bin, we vary (some of) the HOD parameters to fit the measured $b_{(1)}(z)$, thus getting a model for $b_{(1)}^h(z)$. We then compute $b_{(2)}^h(z)$ using as an additional ingredient the following relation between the first and second-order halo bias, which approximates the results from separate universe simulations (Lazeyras et al. 2016) within the fitting range $1 \lesssim b_{(1)}^h \lesssim 10$:

$$b_{(2)}^h(M, z) = 0.412 - 2.143 b_{(1)}^h(M, z) + 0.929 [b_{(1)}^h(M, z)]^2 + 0.008 [b_{(1)}^h(M, z)]^3. \quad (42)$$

Finally, we plug the $b_{(2)}^h$ values obtained in this way back into Eq. (40) to get the second-order galaxy bias. The details of the HMF and HOD used and of the fitting procedure are given in Appendix B.

3.7. Data vectors and Fisher matrix

Up to now, we have been fully general without making any assumptions about the data. We now need to set data-related quantities.

First, we assume to measure $C_{ij}^{AB}(\ell)$ in 10 equipopulated redshift bins over the redshift range (0.001, 2.5). When integrating Eq. (1) in dz , z_{max} must be larger than the upper limit of the last redshift bin to account for the broadening of the bin redshift distribution due to photo- z uncertainties. We have found that the $C_{ij}^{AB}(\ell)$ stop varying for $z_{\text{max}} \geq 4$, which is what we take as the upper limit in the integrals over z . This also means that we need to extrapolate the bias beyond the upper limit of the last redshift bin; we then take its value as constant and equal to the one in the last redshift bin, that is, $b(z > 2.501) = b_{10}$.

Second, we assume the same multipole limits as in EC20, hence examining two scenarios, namely

- *pessimistic*:

$$(\ell_{\text{min}}, \ell_{\text{max}}) = \begin{cases} (10, 1500) & \text{for WL} \\ (10, 750) & \text{for GCph and XC} \end{cases},$$

- *optimistic*:

$$(\ell_{\text{min}}, \ell_{\text{max}}) = \begin{cases} (10, 5000) & \text{for WL} \\ (10, 3000) & \text{for GCph and XC} \end{cases}.$$

Then, for the multipole binning, instead of dividing these ranges into \mathcal{N}_ℓ (logarithmically equispaced) bins in all cases as is done in EC20, we follow the most recent prescriptions of the EC and proceed as follows:

- we fix the centers and edges of 32 bins (as opposed to 30) in the ℓ range [10, 5000] following the procedure described in Appendix C. This will be the ℓ configuration of the optimistic WL case.
- The bins for the cases with $\ell_{\text{max}} < 5000$, such as WL pessimistic, GCph or XC, are obtained by cutting the bins of the optimistic WL case with $\ell_{\text{center}} > \ell_{\text{max}}$. This means that instead of fixing the number of bins and having different bins' centers and edges as done in EC20, we fix the bins' centers and edges and use a different number of bins, resulting in, e.g., $\mathcal{N}_\ell^{\text{WL}} > \mathcal{N}_\ell^{\text{GCph}}$.

The number of multipole bins is then $\mathcal{N}_\ell^{\text{WL}} = 26$ and $\mathcal{N}_\ell^{\text{GCph}} = \mathcal{N}_\ell^{\text{XC}} = 22$ in the pessimistic case and $\mathcal{N}_\ell^{\text{WL}} = 32$ and $\mathcal{N}_\ell^{\text{GCph}} = \mathcal{N}_\ell^{\text{XC}} = 29$ in the optimistic case. In all these cases, the angular PS are computed at the center of the ℓ bin. As mentioned, we will consider the different probes in isolation, as well as combine them in the '3×2pt' analysis, which includes three 2-point angular correlation functions (in harmonic space): $C_{ij}^{\text{LL}}(\ell)$, $C_{ij}^{\text{GL}}(\ell)$ and $C_{ij}^{\text{GG}}(\ell)$. The ℓ binning for the 3×2pt case is the same as for the GCph one.

The covariance matrix and the derivatives of the data vector w.r.t. the model parameters are the only elements needed to compute the FM elements. The one-dimensional data vector \mathcal{C} is constructed by simply compressing the redshift and multipole indices (and, in the 3×2pt case, the probe indices) into a single one, which we call p (or q). For Gaussian-distributed data with a parameter-independent covariance, the FM is given by:

$$F_{\alpha\beta} = \frac{\partial \mathcal{C}}{\partial \theta_\alpha} \text{Cov}^{-1} \frac{\partial \mathcal{C}}{\partial \theta_\beta} = \sum_{pq} \frac{\partial \mathcal{C}_p}{\partial \theta_\alpha} \text{Cov}_{pq}^{-1} \frac{\partial \mathcal{C}_q}{\partial \theta_\beta}, \quad (43)$$

We note that the size of the 3×2pt covariance matrix quickly becomes large. For a standard setting with $\mathcal{N}_b = 10$ redshift bins there are respectively (55, 100, 55) independent redshift bin pairs for (WL, XC, GCph), to be multiplied by the different \mathcal{N}_ℓ . In general, Cov will be a $\mathcal{N}_C \times \mathcal{N}_C$ matrix with

$$\begin{aligned} \mathcal{N}_C &= \left[\mathcal{N}_b(\mathcal{N}_b + 1)/2 \right] \left[\mathcal{N}_\ell^{\text{WL}} + \mathcal{N}_\ell^{\text{GCph}} \right] + \mathcal{N}_b^2 \mathcal{N}_\ell^{\text{XC}} \\ &= \left[\mathcal{N}_b(\mathcal{N}_b + 1) + \mathcal{N}_b^2 \right] \mathcal{N}_\ell^{3 \times 2 \text{pt}}, \end{aligned} \quad (44)$$

for the 3×2pt – where the second line represents the case with the same number of ℓ bins for all probes, which is the one under study – and

$$\mathcal{N}_C = [\mathcal{N}_b(\mathcal{N}_b + 1)/2] \mathcal{N}_\ell^{\text{WL/GCph}}. \quad (45)$$

for the WL and GCph cases. As an example, we will have $\mathcal{N}_C^{3 \times 2 \text{pt, opt}} = 6090$.

Being diagonal in ℓ , most elements of this matrix will be null in the Gaussian case. As shown in Fig. 3, this is no longer true with the inclusion of the SSC contribution, which makes the matrix computation much more resource-intensive. The use of the Numba JIT compiler¹⁰ can dramatically reduce the CPU time from about 260 s to about 2.5 s for the Gaussian + SSC 3×2pt covariance matrix (the largest under study) on a normal laptop working in single-core mode.

Given the highly non-diagonal nature of the Gaussian + SSC covariance, we can wonder whether the inversion of this matrix

¹⁰<https://numba.pydata.org>

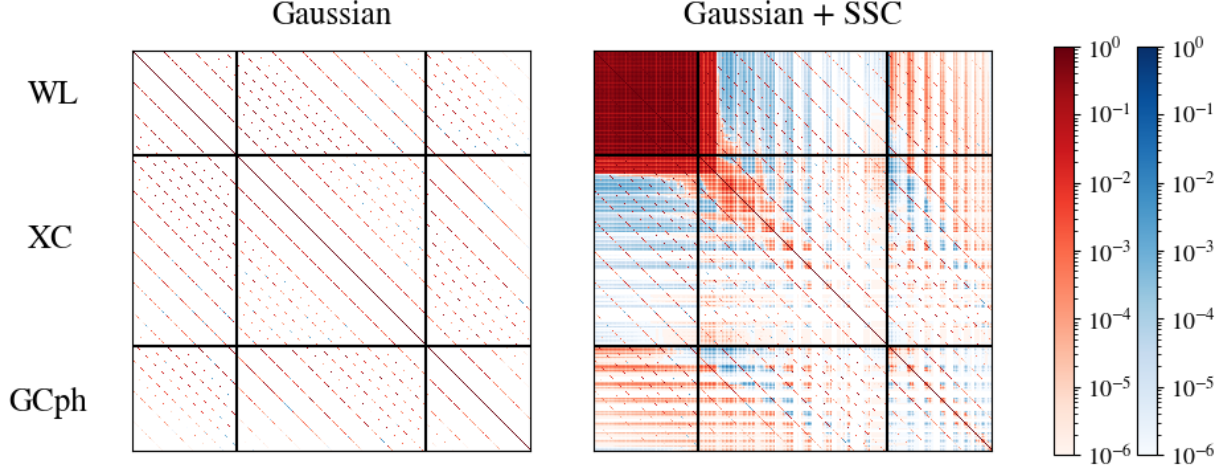


Fig. 3. Correlation matrix in log scale for all the statistics of the 3×2pt data-vector in the G and GS cases. The positive and negative elements are shown in red and blue, respectively. The Gaussian covariance is block diagonal (i.e., it is diagonal in the multipole indices, but not in the redshift ones; the different diagonals appearing in the plot correspond to the different redshift pair indices, for $\ell_1 = \ell_2$). The overlap in the WL kernels makes the WL block in the Gaussian + SSC covariance matrix much more dense than the GCph one.

(which is needed to obtain the FM, see Eq.43) is stable. To investigate this, we compute the condition number of the covariance, which is defined as the ratio between its largest and smallest eigenvalues and in this case of order 10^{13} . This condition number, multiplied by the standard `numpy float64` resolution (2.22×10^{-16}), gives us the minimum precision that we have on the inversion of the matrix, of about 10^{-3} . This means that numerical noise in the matrix inversion can cause, at most, errors of order 10^{-3} on the inverse matrix. Hence, we consider the inversion to be stable for the purpose of this work.

4. Forecast code validation

In order to validate the SSC computation with PySSC, we compare the 1σ forecast uncertainties (which correspond to a 68.3% probability, due to the assumptions of the FM analysis) obtained using two different codes independently developed by two groups, which we call A and B. To produce the FM and the elements needed for its computation (the observables, their derivatives and the covariance matrix), group A uses a private¹¹ code fully written in Python and group B uses CosmoSIS¹² (Jennings et al. 2016). As stated in the introduction, the only shared feature of the two pipelines is the use of PySSC (to compute the S_{ijkl} matrix). For this reason, and because the SSC is not considered in isolation but added to the Gaussian covariance, we compare the forecast results of the two groups both for the Gaussian and Gaussian + SSC cases.

Following EC20, we consider the results to be in agreement if the discrepancy of each group’s results with respect to the median – which in our case equals the mean – is smaller than 10%. This simply means that the A and B pipelines’ outputs are considered validated against each other if

$$\left| \frac{\sigma_\alpha^i}{\sigma_\alpha^m} - 1 \right| < 0.1 \quad \text{for } i = A, B; \quad \sigma_\alpha^m = \frac{\sigma_\alpha^A + \sigma_\alpha^B}{2}, \quad (46)$$

with σ_α^A the 1σ uncertainty on the parameter α for group A. The above discrepancies are equal and opposite in sign for A and B.

¹¹ Available upon request to the author, Davide Sciotti

¹² <https://bitbucket.org/joezuntz/cosmosis/wiki/Home>

The *marginalised* uncertainties are extracted from the FM $F_{\alpha\beta}$, which is the inverse of the covariance matrix $C_{\alpha\beta}$ of the parameters: $(F^{-1})_{\alpha\beta} = C_{\alpha\beta}$. The *unmarginalised*, or conditional, uncertainties are instead given by $\sigma_\alpha^{\text{unmarg.}} = \sqrt{1/F_{\alpha\alpha}}$. We then have

$$\sigma_\alpha = \sigma_\alpha^{\text{marg.}} = \sqrt{(F^{-1})_{\alpha\alpha}}. \quad (47)$$

The uncertainties found in the FM formalism constitute lower bounds, or optimistic estimates, on the actual parameters’ uncertainties, as stated by the Cramér-Rao inequality.

In the following, we normalize σ_α by the fiducial value of the parameter θ_α , in order to work with relative uncertainties: $\bar{\sigma}_\alpha^i = \sigma_\alpha^i / \theta_\alpha^{\text{fid}}$, $\bar{\sigma}_\alpha^m = \sigma_\alpha^m / \theta_\alpha^{\text{fid}}$, again with $i = A, B$. If a given parameter has a fiducial value of 0, such as w_a , we simply take the absolute uncertainty. The different cases under examination are dubbed ‘G’, or ‘Gaussian’, and ‘GS’, or ‘Gaussian + SSC’. The computation of the parameters constraints differs between these two cases only by the covariance matrix used in Eq. (43) to compute the FM

$$\text{Cov} = \begin{cases} \text{Cov}_G & \text{Gaussian} \\ \text{Cov}_{\text{GS}} = \text{Cov}_G + \text{Cov}_{\text{SSC}} & \text{Gaussian + SSC} \end{cases}. \quad (48)$$

As mentioned before, we repeat the analysis for both *Euclid*’s photometric probes taken individually, WL and GCph, as well as for the combination of WL, GCph and their cross-correlation XC, the 3×2pt.

For the reader wanting to validate their own code, we describe the validation process in Appendix A. Here we sketch the results of the code validation: in Fig. 4, we show the percent discrepancy as defined in Eq. (46) for the 3×2pt case. Similar results have been obtained for the GCph and WL cases, both for the optimistic and pessimistic settings specified in Sect. 3.7. The constraints are all found to satisfy the required agreement level (less than 10% discrepancy with respect to the mean). In light of these results, we consider the two forecasting pipelines validated against each other. All the results presented in this paper are the ones produced by group A.

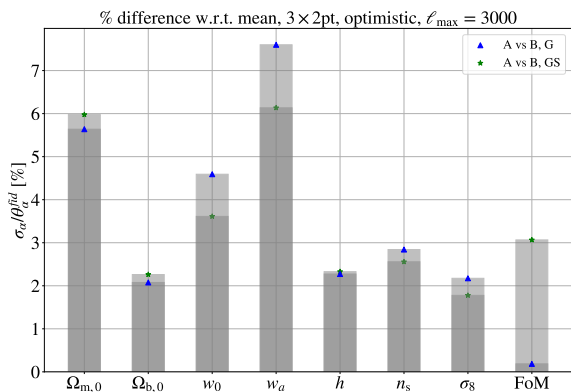


Fig. 4. Percent discrepancy of the normalized 1σ uncertainties with respect to the mean for the WL probe, both in the G and GS cases (optimistic settings). The index $i = A, B$ indicates the two pipelines, whilst α indexes the cosmological parameter. The desired agreement level is reached in all cases (WL, GCph probes and pessimistic case not shown).

5. SSC impact on forecasts

We investigate here how the inclusion of SSC degrades the constraints with respect to the Gaussian case. To this end, we will look in the following at the quantity

$$\mathcal{R}(\theta) = \sigma_{\text{GS}}(\theta) / \sigma_{\text{G}}(\theta), \quad (49)$$

where $\sigma_{\text{G}}(\theta)$ and $\sigma_{\text{GS}}(\theta)$ are the usual marginalised uncertainties on the parameter θ computed, as detailed above, with Gaussian or Gaussian + SSC covariance matrix. We run θ over the set of cosmological parameters listed in Eq. (27), i.e., $\theta \in \{\Omega_{\text{m},0}, \Omega_{\text{b},0}, w_0, w_a, h, n_s, \sigma_8\}$.

In addition we examine the Figure of Merit (FoM) as defined in Albrecht et al. (2006), a useful way to quantify the joint uncertainty on several parameters. We parameterize the FoM following EC20 to focus on the joint uncertainty on the dark energy equation of state parameters w_0 and w_a , such that

$$\text{FoM} = \sqrt{\det(\tilde{F}_{w_0 w_a})}. \quad (50)$$

This quantity is inversely proportional to the area of the 2σ confidence ellipse in the plane spanned by the parameters (w_0, w_a) . $\tilde{F}_{w_0 w_a}$ is the Fisher sub-matrix obtained by marginalising over all the parameters but w_0 and w_a , and is computed by inverting $F_{\alpha\beta}$ (that is, taking the parameters' covariance matrix), removing all the rows and columns but the ones corresponding to w_0 and w_a and re-inverting the resulting 2×2 matrix.

We will also use the notation $\mathcal{R}(\text{FoM})$ as a shorthand for $\text{FoM}_{\text{GS}}/\text{FoM}_{\text{G}}$. We note that, since we expect the uncertainties to be larger for the GS case, we will have $\mathcal{R}(\theta) > 1$, and the FoM being inversely proportional to the area of the uncertainty ellipse, $\mathcal{R}(\text{FoM}) < 1$.

5.1. Reference scenario

Let us start by considering the case with $N_b = 10$ equipopulated redshift bins, which we will take in the following as a reference. Table 1 gives the values of the \mathcal{R} ratios for the different parameters and the FoM in both the pessimistic and optimistic scenarios, for the single or combined probes.

In accordance with previous results in the literature (see e.g. Barreira et al. 2018a; Upham et al. 2022), we find that

the WL constraints are dramatically affected by the inclusion of SSC. The impact is so severe that the FoM is reduced by a factor of about 2 in both the pessimistic and optimistic scenarios. The marginalised uncertainties worsen by a large factor for those parameters which correlate the most with the amplitude of the signal: indeed, the largest $\mathcal{R}(\theta)$ values are obtained for $(\Omega_{\text{m},0}, \sigma_8)$, while $\mathcal{R}(\theta)$ does not meaningfully deviate from unity for $\theta = (w_a, h, n_s)$, and w_0 sits in between the two extreme cases. This is because the SSC effect is essentially an unknown shift, or perturbation, in the background density.

The results in Table 1 also show that GCph is not as strongly affected by SSC. This is an expected result, being the GCph probe response coefficients lower (in absolute value) than the WL ones, as can be seen in Fig. 1. This is due to the additional terms that account for the response of the galaxy number density n_g (see Eq. 14), which is itself affected by the super-survey modes. Moreover, the constraints from GCph alone are obtained by marginalising over a larger number of nuisance parameters than WL – the galaxy bias parameters, which are strongly degenerate with the amplitude of the signal. This works as a sort of effective systematic covariance which makes the SSC less dominant than in the WL case. Lastly, as can be seen from Fig. 2, all WL kernels have non-zero values for $z \rightarrow 0$, contrary to the GCph ones. In this limit, the effective volume probed by the survey tends to 0, hence making the variance of the background modes σ^2 tend to infinity. We thus have a larger S_{ijkl} matrix, which is one of the main factors driving the amplitude of the SSC.

We nevertheless note a 17% decrease of the FoM in the GCph optimistic case, which is related to the inclusion of non-linear modes that are more sensitive to the SSC, as we discuss later.

The full 3×2 pt case sits in between the two extremes as a consequence of the data vector containing the strongly affected WL probe, and the less affected GCph one. The contribution from the XC probe is again an intermediate case because of its lower response coefficient, so the final impact on the FM elements will be intermediate between the WL and GCph cases, as the $\mathcal{R}(\theta)$ values in Table 1 indeed show.

Comparing the optimistic and the pessimistic cases for the two individual probes, we can see that there is a different behaviour of the SSC as a function of the maximum multipole. Indeed, for WL the $\mathcal{R}(\theta)$ ratio for the most affected¹³ parameters is larger in the pessimistic than in the optimistic case. This is consistent with the results of Upham et al. (2022) showing that the diagonal elements of the WL total covariance matrix are more and more dominated by the Gaussian term as we move to higher ℓ . This is because of the presence of the scale-independent shape noise in the Gaussian covariance (see Eq. 24 for $A = B = \text{L}$), which largely dominates over the SSC on small scales. As such, the relative importance of off-diagonal correlations decreases at large ℓ which is precisely what happens when moving from the pessimistic to the optimistic case. This causes the SSC impact to be smaller in the optimistic case, although we note that the $\mathcal{R}(\theta)$ are still remarkably large. Indeed, the \mathcal{R} values for the FoM are roughly the same, pointing to the importance of SSC in both scenarios.

As also seen in Lacasa (2020), we observe the opposite behaviour for the GCph probe, which is more impacted by the SSC in the optimistic case. This is because the impact of the shot

¹³This is not the case for the unconstrained parameters, but the small difference is likely related to numerical artifacts.

Table 1. Ratio between the GS and G constraints for all cosmological parameters and the FoM in the reference scenario, for both pessimistic and optimistic assumptions. We remind the reader that in the reference case, we marginalize over the galaxy bias nuisance parameters while holding the multiplicative shear bias ones fixed.

$\mathcal{R}(x)$	$\Omega_{m,0}$	$\Omega_{b,0}$	w_0	w_a	h	n_s	σ_8	FoM
WL, Pessimistic	1.998	1.001	1.471	1.069	1.052	1.003	1.610	0.475
WL, Optimistic	1.574	1.013	1.242	1.035	1.064	1.001	1.280	0.451
GCph, Pessimistic	1.002	1.002	1.003	1.003	1.001	1.001	1.001	0.996
GCph, Optimistic	1.069	1.016	1.147	1.096	1.004	1.028	1.226	0.833
3×2pt, Pessimistic	1.442	1.034	1.378	1.207	1.028	1.009	1.273	0.599
3×2pt, Optimistic	1.369	1.004	1.226	1.205	1.018	1.030	1.242	0.622

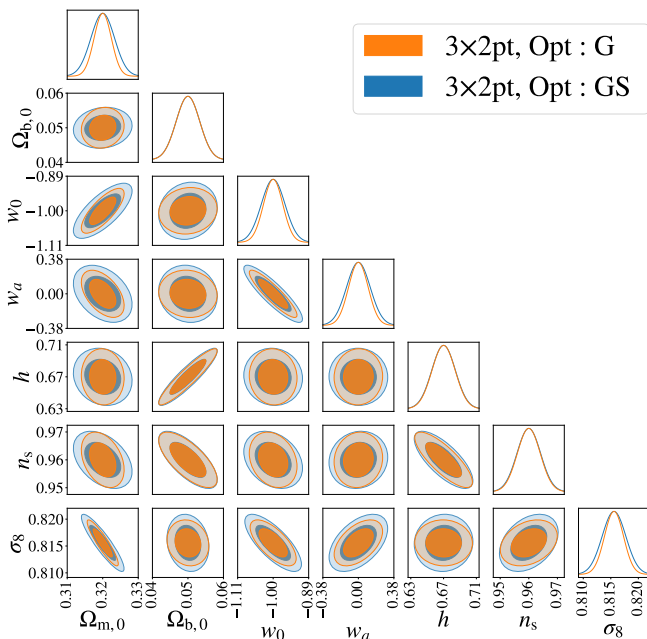


Fig. 5. Contour plot for the G and GS constraints, considering the full 3×2pt analysis in the optimistic case, in the reference scenario. For clarity, the nuisance parameters are shown separately in Fig. 6.

noise at these scales is lower than the shape noise for WL, so the SSC still dominates in that multipole range.

In Fig. 5 we show the comparison of the 2D contours for all cosmological parameters between G and GS in the case of the 3×2pt analysis, in the optimistic case. Again, we can clearly see that the most impacted parameters are $\theta = (\Omega_{m,0}, w_0, \sigma_8)$. In addition, this shows that SSC does not seem to strongly affect the correlations between cosmological parameters.

To conclude this section, it is also worth looking at the impact of SSC on the astrophysical nuisance parameters. Indeed, although an issue to be marginalised over when looking at cosmological ones, the IA and the galaxy bias parameters are of astrophysical interest. We show the impact of SSC on the constraints on these quantities in Fig. 6, and, as an anticipation of the next section, we also show the constraints for other WL-related nuisance parameters, the multiplicative shear bias parameters m_i .

For IA-related nuisance parameters, the uncertainty increase due to SSC is lower than 0.5%. The uncertainty on b_i and m_i in each of the ten redshift bins is however significantly affected by SSC, showing an increase between 1 and 14% for b_i and between

1 and 18% for m_i , depending on the probe combination choice. This is because both of these nuisance parameters simply act as a multiplicative factor on the power spectrum and are thus highly degenerated with the effect of SSC. Again, this is because the first-order effect of SSC is to modulate the overall clustering amplitude because of a shift in the background density δ_b . As mentioned, this cross-talk between SSC and linear galaxy bias could also explain why the GCph probe seems less affected by SSC: some of the difference between G and GS is absorbed by the b_i in the marginalisation. This will be also confirmed for WL in the next section, showing a reduced relative impact of SSC in the presence of multiplicative shear bias. Note that going beyond the linear approximation for the modelling of the galaxy bias will add more nuisance parameters, thus degrading the overall constraints on cosmological parameters and further reducing the relative degradation of constraints due to SSC.

Finally, comparing how uncertainties on b_i and m_i react to the addition of SSC, we can see that surprisingly the b_i are more affected in the 3×2pt case than in the GCph case, while it is the contrary for m_i , the uncertainty increase is larger for WL than for 3×2pt. This difference in the behaviour of the uncertainty increase might come from the numerous degeneracies existing between these nuisance parameters and the most constrained cosmological parameters in each case. Though it is not easy to exactly understand this behaviour, we note that in all cases the $\mathcal{R}(\theta)$ for these parameters are of the same order of magnitude and are never completely negligible.

5.2. Non-flat cosmologies

In the previous section, we investigated the SSC on the cosmological parameters under the assumption of a flat model. Actually, the requirement on the FoM assessed in the *Euclid* Red Book (Laureijs et al. 2011) refers to the case with the curvature as an additional free parameter to be constrained, i.e., the non-flat $w_0 w_a$ CDM model. This is why in EC20 are also reported the marginalised uncertainties for the parameter $\Omega_{DE,0}$, with a fiducial value $\Omega_{DE,0}^{\text{fid}} = 1 - \Omega_{m,0}$ to be consistent with a flat universe. It is worth wondering which is the impact of SSC in this case too. This is summarised in Table 2, where we now also include the impact on $\Omega_{DE,0}$.

A comparison with the results in Table 1 is quite hard if we look at the single parameters. Indeed, opening up the parameter space by removing the flatness assumption introduces additional degeneracy among the parameters controlling the background expansion, which are thus less constrained whether SSC is included or not. We can nevertheless note again that WL is still the most impacted probe, while GCph is less affected, and the 3×2pt sits in between. The difference between pessimistic and

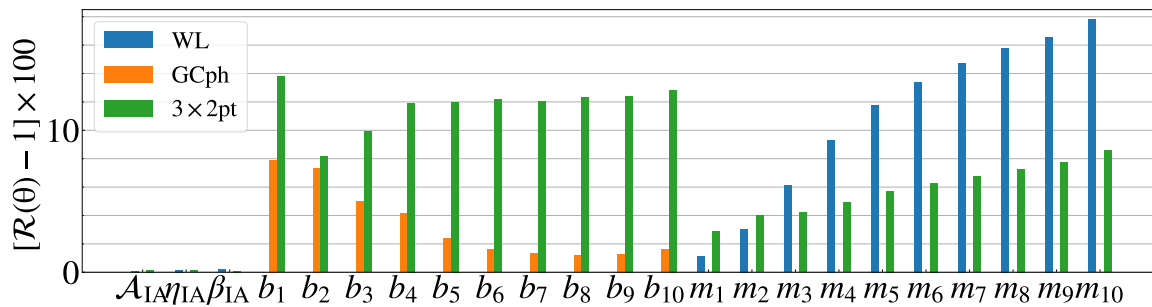


Fig. 6. Percent increase of the marginalised 1σ uncertainty of the nuisance parameters, for all probe choices, in the optimistic case and for the reference scenario.

Table 2. Same as Table 1 but removing the flatness prior.

$\mathcal{R}(x)$	$\Omega_{m,0}$	$\Omega_{DE,0}$	$\Omega_{b,0}$	w_0	w_a	h	n_s	σ_8	FoM
WL, Pessimistic	2.561	1.358	1.013	1.940	1.422	1.064	1.021	1.433	0.514
WL, Optimistic	2.113	1.362	1.004	1.583	1.299	1.109	1.038	1.559	0.631
GCph, Pessimistic	1.002	1.001	1.002	1.002	1.003	1.001	1.000	1.001	0.996
GCph, Optimistic	1.013	1.020	1.006	1.153	1.089	1.004	1.039	1.063	0.831
3×2pt, Pessimistic	1.360	1.087	1.043	1.408	1.179	1.021	1.009	1.040	0.677
3×2pt, Optimistic	1.572	1.206	1.013	1.282	1.191	1.013	1.008	1.156	0.756

optimistic scenarios is now less evident with $\mathcal{R}(\theta)$ increasing or decreasing depending on the parameter and the probe.

Once more, the most affected parameters for WL are $(\Omega_{m,0}, \sigma_8)$, the uncertainties on which are now further degraded by the fact that they correlate with the parameter $\Omega_{DE,0}$ which is also affected. Although (w_0, w_a) are also degraded by the SSC, a sort of compensation is at work, so that the overall decrease in the FoM is similar to the case with the flatness prior. The motivations that make GCph much less affected still hold when dropping the flatness prior, explaining the corresponding $\mathcal{R}(\theta)$ values.

We also note an increase of $\mathcal{R}(\text{FoM})$ in the 3×2pt case, meaning a smaller degradation of the FoM due to SSC. The FoM indeed degrades by 24% (32%) in the non-flat case vs. 38% (40%) for the flat case in the optimistic (pessimistic) scenario. This can be qualitatively explained by noting that the decrease of both FoM(G) and FoM(GS) is related to a geometrical degeneracy which is the same on all scales, whether or not they are affected by the increase in uncertainty due to the SSC inclusion.

5.3. Role of nuisance parameters

We can now open up the parameter space by letting the shear bias parameters introduced in Sect. 3.6 free to vary. We expand the FM by adding these additional parameters and recompute the ratios of uncertainties with and without SSC obtaining the results shown¹⁴ in Table 3. We remind the reader that the number of nuisance parameters depends on which probe (WL or 3×2pt) one is considering. For the WL case, the \mathcal{N}_b multiplicative shear bias parameters add up to the 3 IA ones leading to the result that the SSC has a very minor impact on the constraints and on the FoM. The values in Table 3 are actually easily explained. We recall that $\mathcal{R}(\theta)$ is a ratio between the constraints with and without the SSC. Adding m_i to the cosmological parameters introduces a de-

generacy between m_i itself and the parameters $(\Omega_{m,0}, \sigma_8)$ which set the overall amplitude of $C_{ij}^{LL}(\ell)$. Such a degeneracy is a mathematical one present on the whole ℓ range, similar to the galaxy bias parameters for GCph. As a consequence, the constraints on all the parameters and the FoM are strongly degraded in a way that is independent of the presence of SSC. This is shown in Fig. 7 and 8, which exhibits the relative uncertainty $\bar{\sigma}$ and the dark energy FoMs in the G and GS cases for each parameter, if we marginalise or not on over nuisance parameters. Letting the nuisance parameters free to vary, i.e. marginalising over them, tends to increase the uncertainty on cosmological parameters way more than including SSC and this is even more true when these nuisance parameters are simply multiplicative such as b_i and m_i .

This is why the \mathcal{R} values drop down to values close to unity when m_i are varied, in contrast to what we have found up to now for WL. Introducing more nuisance parameters degenerated with the amplitude of the signal dilutes the SSC effect in a larger error budget; because of this, it is the relative rather than the absolute impact of SSC that decreases. Indeed, marginalising over nuisance parameters is formally equivalent to having additional covariance. Note that this does not mean that adding nuisance parameters improves the constraints. Indeed, the marginalised uncertainties on all parameters increase (hence the FoM decreases) with respect to the case when the multiplicative shear bias is fixed. The degradation is, however, the same with and without SSC so the $\mathcal{R}(\theta)$ values stay close to unity.

On the contrary, the results for the 3×2pt case show that the SSC still matters. The additional information carried by the GCph and XC data allows the partial breaking of the mathematical degeneracy among $(m_i, \Omega_{m,0}, \sigma_8)$ hence making again the scale-dependent increase of the uncertainties due to the inclusion of SSC important. However, the larger number of nuisance parameters (from 13 to 23) still introduces additional degeneracies with the cosmological ones hence alleviating the impact of SSC. The overall effect is, however, small with the \mathcal{R} values being close to the ones in Table 2. In particular, the FoM degrada-

¹⁴We do not report here the results for GCph since they are the same as the ones shown in Table 1, given that $C_{ij}^{GG}(\ell)$ is unaffected by multiplicative shear bias.

Table 3. Same as Table 2 but adding multiplicative shear bias nuisance parameters.

$\mathcal{R}(x)$	$\Omega_{m,0}$	$\Omega_{DE,0}$	$\Omega_{b,0}$	w_0	w_a	h	n_s	σ_8	FoM
WL, Pessimistic	1.082	1.049	1.000	1.057	1.084	1.034	1.025	1.003	0.917
WL, Optimistic	1.110	1.002	1.026	1.022	1.023	1.175	1.129	1.009	0.976
3×2pt, Pessimistic	1.297	1.087	1.060	1.418	1.196	1.021	1.030	1.035	0.674
3×2pt, Optimistic	1.222	1.136	1.010	1.300	1.206	1.013	1.009	1.164	0.745

tion is essentially the same in both the pessimistic and optimistic cases.

Overall, these results suggest a dependence of the SSC significance on both the number and type of parameters to be constrained. Qualitatively, we can argue that SSC is more or less important depending on whether the additional parameters (with respect to the reference case of a flat model with fixed shear bias) introduce degeneracies which are or not scale-dependent and how strong is the degeneracy between these parameters and the amplitude of the power spectrum. In future works lens magnification effects should be included in the analysis as it was shown to have a significant impact on cosmological constraints (Unruh et al. 2020). But from our results we can anticipate that the inclusion of magnification-related nuisance parameters will further dilute the impact of SSC.

5.4. Dependence on redshift binning

The results summarised in Tables 1–3 have been obtained for a fixed choice of number and type of redshift bins. We investigate here how they depend on these settings given that we expect both the G and GS constraints to change as we vary the number and type of bins. We will consider the case of non-flat models, fixing the multiplicative shear bias parameters in order to better highlight the impact of SSC. For this same reason, we will only consider the WL and 3×2pt cases, since SSC has always a modest impact on GCph. Let us first consider changing the number of redshift bins \mathcal{N}_b . We show the scaling of $\mathcal{R}(\theta)$ as a function of \mathcal{N}_b for the WL and 3×2pt probes, respectively, in Fig. 9 – for both the pessimistic and optimistic assumptions. The most remarkable result is the weak dependence of $\mathcal{R}(\text{FoM})$ on \mathcal{N}_b as can be inferred from the small range spanned by the curves in the bottom right panel. The scaling of $\mathcal{R}(\theta)$ with \mathcal{N}_b depends, instead, on the parameter and the probe one is looking at. It is quite hard to explain the observed trends because of the interplay of different contrasting effects. For instance, a larger number of bins implies a smaller number density in each bin, hence a larger shot noise. As a consequence, the SSC contribution to the total covariance for the diagonal elements will likely be more and more dominated by the Gaussian component because of the larger shot and shape noise terms. However, this effect also depends on the scale so that, should the SSC be the dominant component on the scales to which a parameter is most sensitive, the impact should still be important. On the other hand, a larger number of bins also comes with a larger number of nuisance parameters which, as shown above, leads to a reduction of the SSC impact. Quantifying which actor plays the major role is hard which explains the variety of trends in the different panels.

As a further modification to the reference settings, we can change how the redshift bins are defined. We have up to now considered equipopulated (EP) bins so that the central bins cover a smaller range in z , because of the larger source number density. As an alternative, we divide the full redshift range into \mathcal{N}_b bins with equal length (ED), and recompute the FM forecasts with and without SSC. We show the FoM ratio as a function of the

number of bins for EP and ED bins considering WL (left) and 3×2pt (right) probes in the optimistic scenario in Fig. 10. Note that finding the exact number and type of redshift bins used to maximize the constraining power of *Euclid* is outside the scope of this paper; this effort is indeed brought forward in the context of the SPV exercise.

In order to qualitatively explain these results, let us first consider the WL case. Given that the bins are no longer equipopulated, the number density of galaxies will typically be larger in the lower redshift bins than in the higher ones. As a consequence, the larger the number of bins, the higher the shape noise in the higher redshift bins so that the SSC will be subdominant in a larger number of bins, which explains why its impact decreases (i.e., $\mathcal{R}(\text{FoM})$ increases) with \mathcal{N}_b . Nevertheless, the impact of SSC will be larger than in the EP case since SSC will dominate in the low redshift bins which are the ones with the largest S/N. This effect is, however, less important, so although $\mathcal{R}(\text{FoM})$ is smaller for ED than for EP bins, the difference is no larger than 3–5%.

When adding GCph and XC into the game, the impact of SSC is determined by a combination of contrasting effects. On one hand, we can repeat the same qualitative argument made for WL also for GCph thus pointing at $\mathcal{R}(\text{FoM})$ increasing with \mathcal{N}_b . No shape or shot noise is included in the XC Gaussian covariance, which is then only determined by how much shear and position are correlated. The larger the number of bins, the narrower they are, the smaller the cross-correlation between them hence the smaller the Gaussian covariance. This in turn increases the number of elements in the data vector whose uncertainty is dominated by the SSC. Should this effect dominate, we would observe a decrease of $\mathcal{R}(\text{FoM})$ with \mathcal{N}_b with the opposite trend if it is the variation of the shape and shot noise to matter the most. This qualitative argument allows us then to roughly explain the non-monotonic behaviour of $\mathcal{R}(\text{FoM})$ we see in the right panel of Fig. 10. It is worth remarking, however, that the overall change of $\mathcal{R}(\text{FoM})$ for ED bins over the range in \mathcal{N}_b is smaller than $\sim 12\%$ which is also the typical value of the difference between $\mathcal{R}(\text{FoM})$ values for EP and ED bins once \mathcal{N}_b is fixed.

The analysis in this section, therefore, motivates us to argue that the constraints and FoM degradation due to SSC are quite weakly dependent on the redshift binning.

5.5. Requirements on prior information

The results in the previous paragraph show that the SSC may dramatically impact the constraints on the cosmological parameters. As a consequence, the 3×2pt FoM is reduced by up to $\sim 24\%$ with respect to the case when only the Gaussian term is included in the total covariance. This decrease in the FoM should actually not be interpreted as a loss of information due to the addition of the SSC. On the contrary, one can qualitatively say that removing SSC from the error budget is the same as adding information that is not actually there. It is nevertheless interesting to ask which additional information must be added to recover the Gaussian FoM, which is usually taken as a reference for gauging

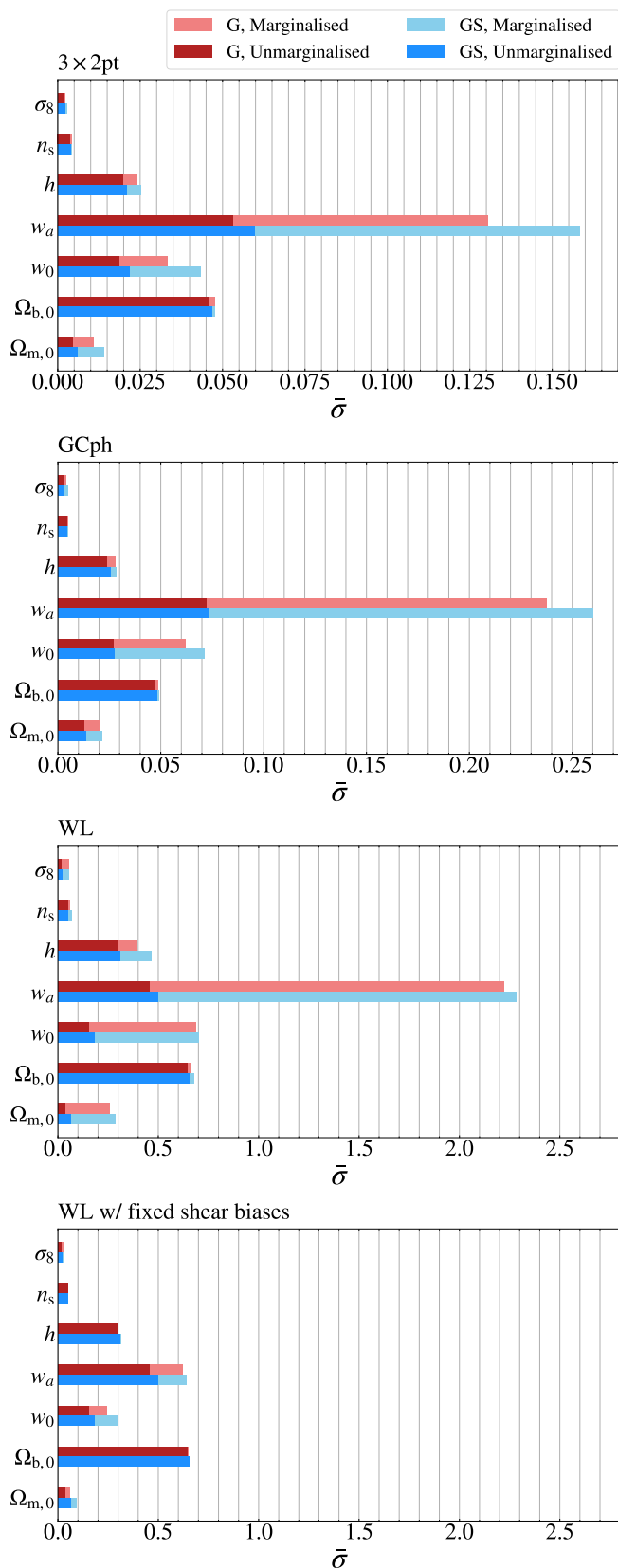


Fig. 7. Marginalised and unmarginalised 1σ uncertainties on the cosmological parameters, relative to their corresponding fiducial values, in both the G and GS cases for 3×2 pt, GCph and WL. For WL we show the results in the case where the shear multiplicative biases are either varied or fixed, in other words whether we marginalise over all nuisance parameters or only over the IA ones.

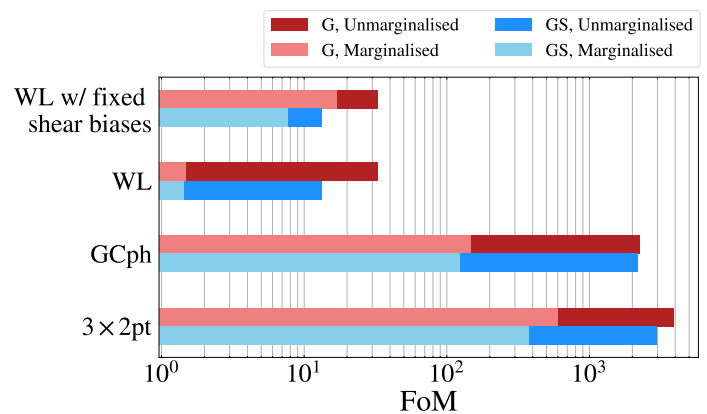


Fig. 8. Dark energy FoM for marginalised and unmarginalised constraints in both the G and GS cases, 3×2 pt, GCph, WL, and WL with fixed shear multiplicative biases.

the potential of a survey. This information can come from priors on the nuisance (or cosmological) parameters. In the following section, we will investigate the former option by adding Gaussian priors on the galaxy and multiplicative shear bias parameters. This is easily done in the FM formalism, by adding $(\sigma_\alpha^p)^{-2}$ to the appropriate diagonal elements of the G and GS FMs (σ_α^p being the value of the prior uncertainty on parameter α).

To this end, we consider the realistic case of a non-flat model plus the galaxy bias and multiplicative shear bias as nuisance parameters. As a simplifying assumption, we will assume that all the \mathcal{N}_b bias values b_i are known with the same percentage uncertainty $\varepsilon_b = \sigma_b/b_{\text{fid}}$, while we put a prior σ_m on all the m_i parameters (having set the fiducial value m_{fid} to 0). We then compute the FoM with and without SSC for the 3×2 pt probe in the optimistic scenario and investigate how the ratio $\mathcal{R}(\text{FoM})$ scales with $(\varepsilon_b, \sigma_m)$ obtaining the results shown in Fig. 11.

A prior on the nuisance parameters increases both the Gaussian and Gaussian + SSC FoM so that one could expect their ratio to be independent of the prior itself. This is not exactly the case since the correlation between different multipoles introduced by SSC alters the way the prior changes the FM elements. As a result, we find a non-flat scaling of $\mathcal{R}(\text{FoM})$ as can be seen from the right panel of Fig. 11. When a strong prior is set on the galaxy bias (i.e., $\varepsilon_b \ll 1$), there is not much gain in improving the knowledge of the multiplicative shear bias so that the solid, dashed, and dotted lines (corresponding to three σ_m values) are quite close to each other. This is no longer the case for larger ε_b values (i.e., weak or no prior on the bias): lowering σ_m has now a larger impact on $\mathcal{R}(\text{FoM})$. The non-monotonic behaviour of $\mathcal{R}(\text{FoM})$ with ε_b tells us that FoM_{GS} increases with decreasing ε_b faster (slower) than FoM_{G} when the galaxy bias is known with an uncertainty smaller (higher) than the sub-percent level. Another way to interpret it is that the information gained in the FoM saturates faster when SSC is included: better constraints on ε_b do not bring more information as the SSC now dominates the error budget. However, it is worth stressing that, even for a strong prior on the multiplicative shear bias, the FoM ratio can actually be improved by less than a few percent under the (likely unrealistic) assumption of a sub-percent prior on the galaxy bias.

The need for such strong priors comes from the attempt to retrieve the same FoM as a Gaussian case. Alternatively, one can also wonder which additional information must be added through priors to retrieve the idealised FoM value obtained in forecasts that neglect the SSC. In other words, we look for the

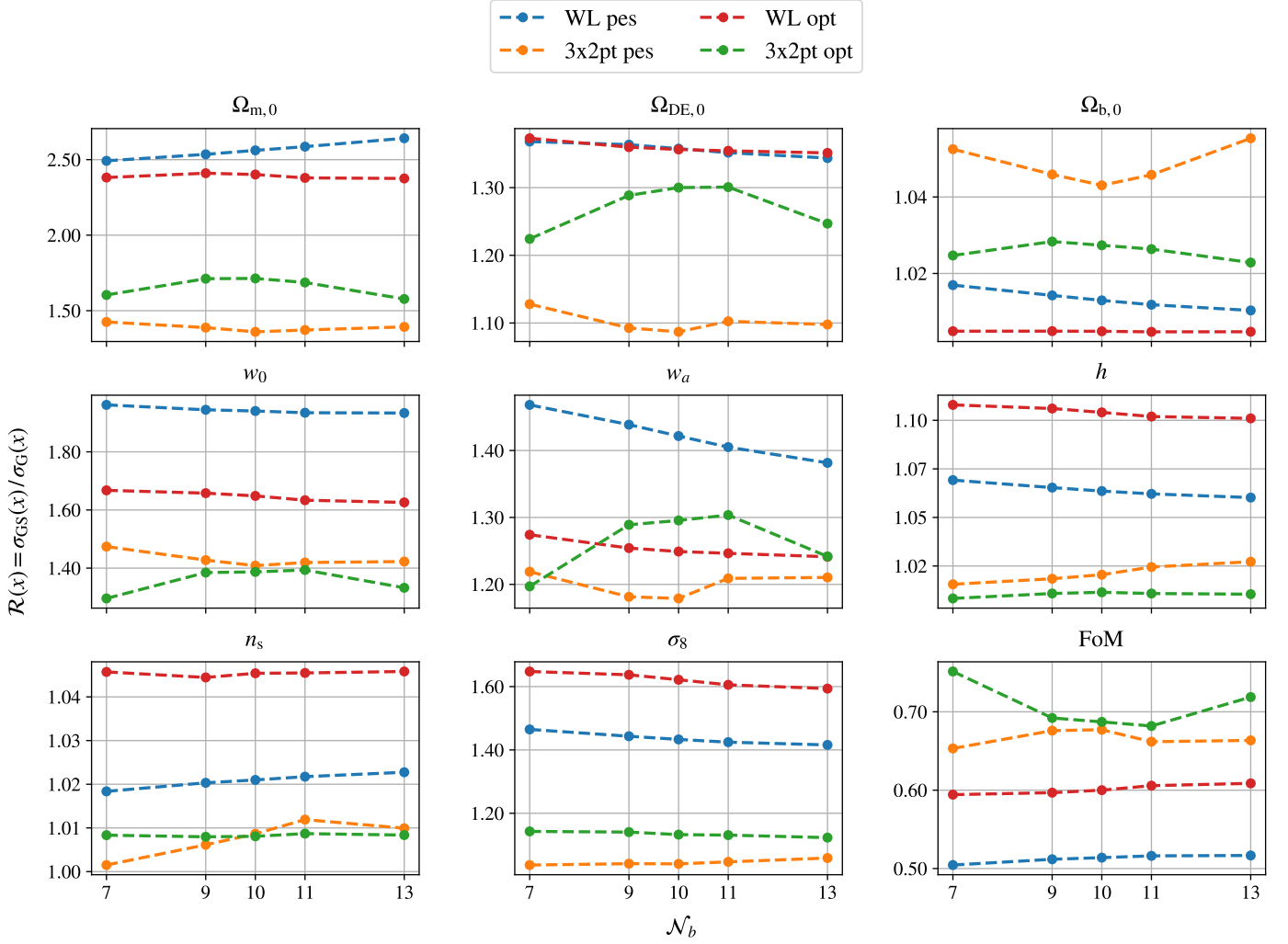


Fig. 9. Ratio between WL and 3×2pt marginalised uncertainties computed by including or neglecting the SSC contribution, as a function of the number of redshift bins, for the pessimistic and optimistic cases.

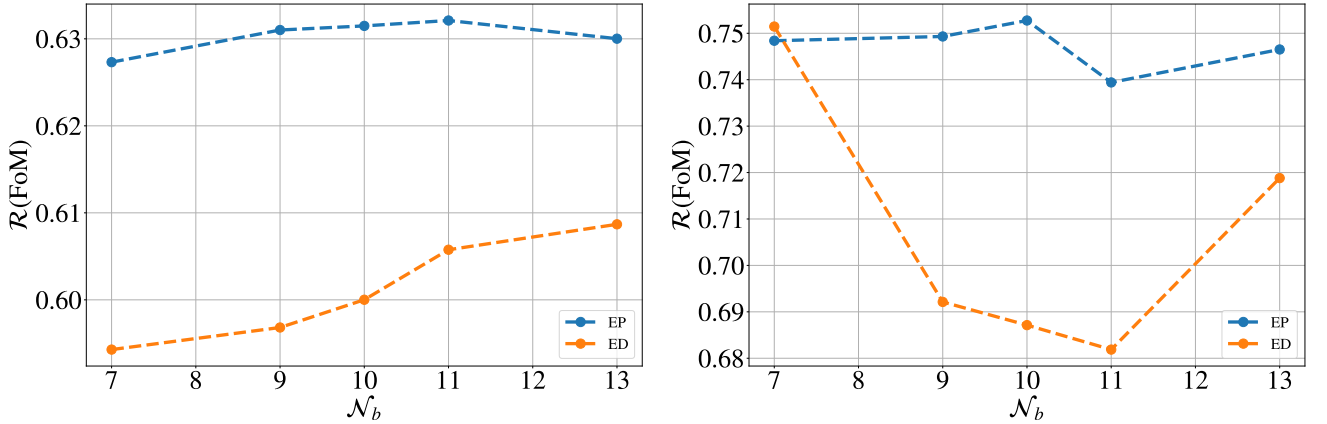


Fig. 10. FoM ratio vs the number of EP and ED redshift bins for WL (left) and 3×2pt (right) in the optimistic scenario.

requirements that must be put on the priors $(\varepsilon_b, \sigma_m)$ in order to make $\text{FoM}_{\text{GS}}/\text{FoM}_{\text{ref}} = 1$, where $\text{FoM}_{\text{ref}} = 295$ is the FoM computed for a non-flat reference case without SSC and with no priors on galaxy bias, but a fiducial prior $\sigma_m = 5 \times 10^{-4}$ on the shear bias. The answer to this question is shown in Fig. 12 for the optimistic scenario and 10 equipopulated redshift bins. Some numbers help to better understand how priors can indeed supply

the additional information to retrieve the FoM one would obtain in an ideal case where SSC is absent. Solving

$$\text{FoM}_{\text{GS}}(\varepsilon_b, \sigma_m) = f \text{FoM}_{\text{ref}}$$

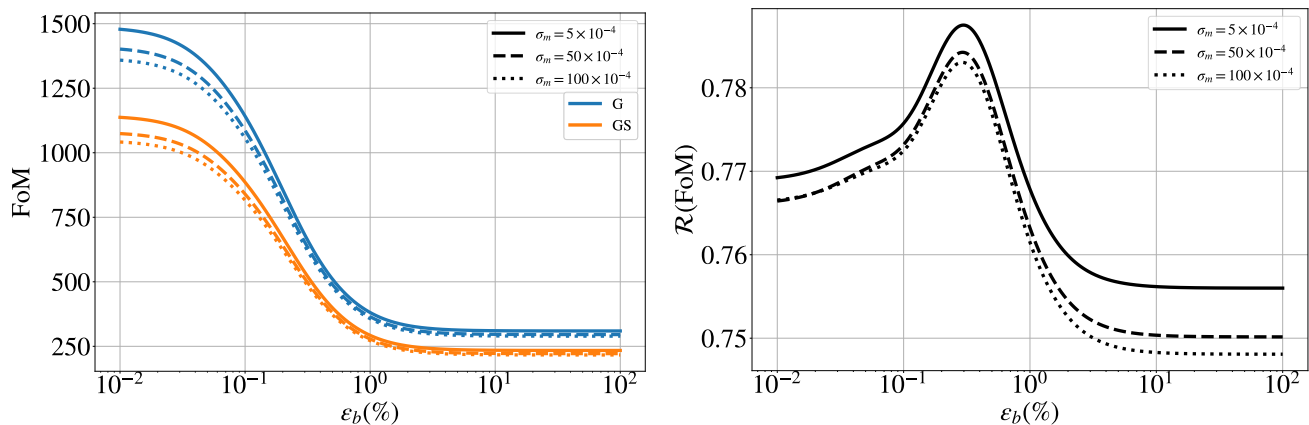


Fig. 11. *Left.* 3×2 pt FoM in the optimistic scenario with and without SSC as a function of the percentage prior ε_b on the galaxy bias parameters for $\sigma_m = (5, 50, 100) \times 10^{-4}$ (solid, dashed, dotted lines). *Right.* FoM ratio as function of ε_b for the three σ_m values in the left panel.

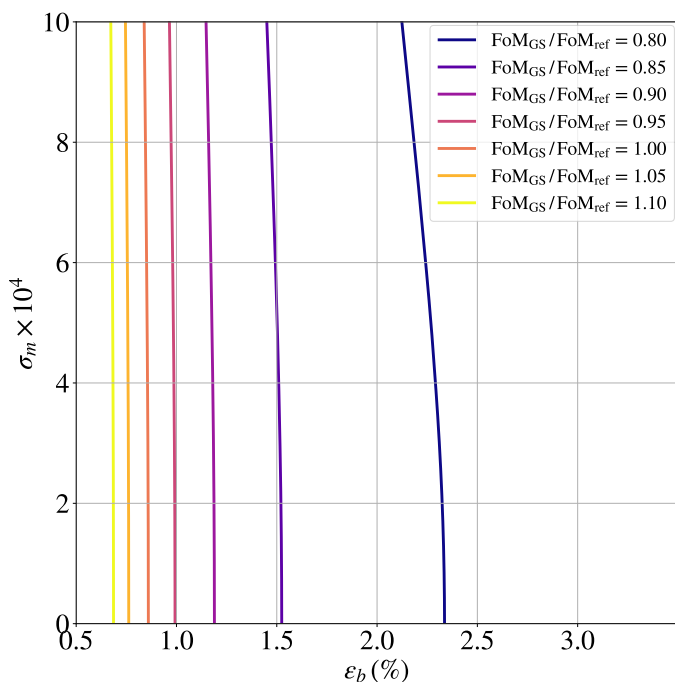


Fig. 12. FoM_{GS} contours in the $(\varepsilon_b, \sigma_m)$ plane for FoM_{GS}/FoM_{ref} going from 0.8 to 1.1 in steps of 0.05 (from right to left).

with respect to ε_b , we get

$$\varepsilon_b = \begin{cases} (2.34, 1.19, 0.86) \% & \text{for } \sigma_m = 0.5 \times 10^{-4} \\ (2.27, 1.18, 0.85) \% & \text{for } \sigma_m = 5 \times 10^{-4} \\ (1.40, 0.93, 0.72) \% & \text{for } \sigma_m = 100 \times 10^{-4}, \end{cases}$$

where the three values refer to $f = (0.8, 0.9, 1.0)$. These numbers (and the contours in Fig. 12) show that it is indeed possible to compensate for the degradation due to SSC by adding strong priors on the galaxy bias, which have a much larger impact on the (G and GS) FoM than strong priors on the multiplicative shear bias. However, it is worth noticing that it is actually easier to obtain priors on the multiplicative shear bias provided a sufficient number of realistic image simulations are produced and fed to the shear measurement code to test its performance. It is therefore worth wondering how much the FoM is restored by improv-

ing the prior on m for a fixed one on the bias. We find

$$\frac{\text{FoM}_{\text{GS}}}{\text{FoM}_{\text{ref}}} = \begin{cases} (2.87, 2.86, 2.64) & \text{for } \varepsilon_b = 0.1\% \\ (0.95, 0.95, 0.88) & \text{for } \varepsilon_b = 1\% \\ (0.76, 0.76, 0.70) & \text{for } \varepsilon_b = 10\%, \end{cases}$$

with the three values referring to $\sigma_m = (0.5, 5.0, 100) \times 10^{-4}$. As expected, improving the prior on the multiplicative bias with respect to the fiducial one (which, we remind, is included in FoM_{ref}) does not help a lot in recovering the constraining power. However, a 1% prior on the galaxy bias can almost fully recover the reference FoM thanks to the additional information compensating for the presence of SSC.

Investigating whether the priors proposed here can be achieved in practice (e.g., through theoretical bias models tailored to galaxy clustering data or N-body hydrodynamic simulations) is outside the aim of this work. We refer the interested reader to, e.g., Barreira et al. (2021) and Zennaro et al. (2022) for some preliminary results.

6. Conclusions

Precision cosmology asks for precision computation too: previously neglected theoretical contributions must therefore now be taken into account. Motivated by this consideration, we have here computed and studied the impact of SSC on the *Euclid* photometric survey, exploring how the different probes and their combination are affected by this additional, non-Gaussian term in the covariance matrix. The analysis of the impact of SSC on the spectroscopic survey, which has been shown to be small in Wadekar et al. (2020) for the Baryon Oscillation Spectroscopic Survey (BOSS) data, is left for future work. We employed a FM analysis, producing forecasts of the 1σ marginalised uncertainties on the measurement of the cosmological parameters of the flat and non-flat $w_0 w_a$ CDM cosmological models. We validated two different forecast pipelines against the results of EC20, taking as reference survey the one specified therein, and then updated the galaxy bias and the source redshift distributions according to the most recent versions presented in Euclid Collaboration: Pocino et al. (2021). The SSC was computed relying on the analytical approximations and numerical routines presented in LG19, interfacing the public code PySSC with two distinct forecast pipelines to validate the constraints. As a further

step forward, we build upon the work of LG19 by computing the scale and redshift dependence of the response functions of the different probes, starting from the results of Wagner et al. (2015b) and Barreira et al. (2018b).

We find the severity of the impact, quantified by the ratio σ_{GS}/σ_G between the marginalised uncertainties with and without SSC, to vary substantially between different parameters and probes. For both WL and GCph, the most affected parameters are $(\Omega_{m,0}, w_0, \sigma_8)$, while the constraints on $(\Omega_{b,0}, h, n_s)$ are only weakly degraded by SSC. However, there is a great difference between the two probes in how much the constraints worsen because of SSC. In agreement with previous results (Upham et al. 2022; Barreira et al. 2018a), we found the WL case to be dramatically impacted by SSC so that the corresponding FoM is reduced by as much as 55%, while GCph is less affected with the FoM decrease being about 17%. The 3×2pt case sits in between these two since it receives contributions from both extreme cases. These results are the consequence of a complicated interplay among three factors. First, SSC originates from the uncertainty in the determination of the background mean density when measuring it over a finite region. This prevents determining the overall amplitude of the matter power spectrum hence increasing the uncertainty on those parameters that concur in setting its amplitude, mainly $\Omega_{m,0}$ and σ_8 . Secondly, the elements of the SSC matrix depend on the amplitude of the response functions. Thirdly, the impact depends on how large a contribution the signal receives from the low- z region, where the effective volume probed is smaller, making the variance of the background modes larger. Both the last two factors are more severe for WL than for GCph, hence causing the former probe to be more affected than the latter.

Finally, the deviation of a given element of the GS FM from the Gaussian one depends also on its correlations: in other words, the degradation of the constraints on a given parameter can be large if this is strongly correlated with a parameter severely degraded by SSC. Quantifying the impact of SSC on a single parameter is therefore quite hard in general, and must be investigated on a case-by-case basis taking care of the details of the probe and the way it depends on the parameter of interest.

Nuisance parameters to be marginalised over act as a sort of additional contribution to the covariance. As such, the importance of both the Gaussian and SSC contribution to the overall effective covariance becomes less important when the number of nuisance parameters increases. In order to consider cases that mimic the most future *Euclid* data, we have opened up the parameter space by adding $\Omega_{DE,0}$ (i.e., removing the flatness prior), and the multiplicative shear bias. It turns out that, as long as the additional parameters have a scale-independent degeneracy with the most impacted ones, the relative impact of SSC decreases. We stress, however, that this reduction in the SSC impact does not come for free. On the contrary, the marginalised uncertainties on the parameters are definitely worsened, but the degradation is roughly the same whether the SSC is included or not, hence making the ratio σ_{GS}/σ_G closer to unity for all parameters and probes. This result can be taken as a warning against investing too much effort in refining the estimate of the computationally expensive SSC when no approximations are done. For a *Euclid*-like survey, the main concern would indeed be the number of nuisance parameters, which makes less relevant the impact of the SSC itself.

We furthermore note, in light of the recent theoretical developments presented in Lacasa et al. (2023), it appears feasible to include the effect of SSC in the form of nuisance parameters which would be the value of the density background δ_b in each

redshift bin. This approach is interesting as it would reduce the complexity of the data covariance matrix and would allow for a simpler interpretation of the effect of SSC and how it is correlated to the other cosmological and nuisance parameters.

Variations in the z binning strategy have contrasting effects: a larger number of bins means a larger number of nuisance parameters (either galaxy bias or multiplicative shear bias for each bin), which leads to a loss of constraining power. Moreover, the larger the number of bins, the larger the Gaussian contribution to the covariance, making the shot and shape noise dominate over SSC for diagonal elements. On the downside, a larger number of bins leads to larger data vectors, thus adding information that can partially compensate for the increase in the covariance. The contrasting effects at play conspire in such a way that the degradation of the FoM due to SSC ends up being approximately independent of the number of redshift bins (cfr. Fig. 10).

An interesting development in this sense is to leverage the SSC dependence on the low- z contribution to investigate whether its impact could be mitigated by the use of the BNT (Bernardeau-Nishimichi-Taruya) transform (Bernardeau et al. 2014), which transforms redshift bins in such a way as to increase the separation between the WL kernels. This will be investigated in a forthcoming work.

An alternative strategy is to increase the constraining power by adding information through informative priors, hence recovering the FoM when SSC is incorrectly neglected. We investigate this possibility by quantifying the requirements on the prior information needed to recover the Gaussian FoM. Our results show that the main role is played here by the priors on galaxy bias parameters, while the FoM recovery quickly saturates with the prior on the multiplicative shear bias. However, the galaxy bias must be known to sub-percent level in order to recover $\sim 90\%$ of the Gaussian FoM. Investigating whether this is possible is outside the scope of this paper. We nevertheless note that such remarkable prior information is the same as stating we are able to model the evolution of the bias with redshift. This is actually quite difficult based on the current knowledge of galaxy formation processes. Alternatively, one could investigate whether an empirical fitting formula can be found as a compromise between the need for strong priors on bias and the number of nuisance parameters.

Although some more work is needed to make the results more robust, e.g. by comparing the different approximations presented in the literature, we can conclude that the effect of including the SSC term in the total covariance matrix of *Euclid* photometric observables is definitely non-negligible, especially for WL and 3×2pt. However, the degradation of the constraints on cosmological parameters depends on the particular probe and the number and kind of parameters to constrain. The FoM is nevertheless reduced by 32% (25%) for the 3×2pt probe in the pessimistic (optimistic) scenario in the case all cosmological (including $\Omega_{DE,0}$) and nuisance (multiplicative shear bias) parameters are left free to vary. Mining most of the gold from the actual *Euclid* photometric data taking into account the presence of SSC is a daunting task which we will report on in a forthcoming publication.

Acknowledgements. The computational part of the work has been performed using the Python programming language, interfaced with scientific packages like *astropy* (Astropy Collaboration: Robitaille et al. 2013; Astropy Collaboration: Price-Whelan et al. 2018) for cosmological calculations, *Numba* (Lam et al. 2015) for code speedup, *NumPy* (Harris et al. 2020) for matrix manipulation, *SciPy* (Virtanen et al. 2020) for numerical integration and *Matplotlib* (Hunter 2007) for data visualization. DS would like to thank Raphael Kou for the fruitful discussion on the SSC impact on GCph. SGB was supported by CNES,

funding on *Euclid* mission. The project leading to this publication has received funding from Excellence Initiative of Aix-Marseille University -A*MIDEX, a French "Investissements d'Avenir" programme (AMX-19-IET-008 -IPhU). SC acknowledges support from the 'Departments of Excellence 2018-2022' Grant (L. 232/2016) awarded by the Italian Ministry of University and Research (MUR). IT acknowledges funding from the European Research Council (ERC) under the European Union's Horizon 2020 research and innovation programme (Grant agreement No. 863929; project title "Testing the law of gravity with novel large-scale structure observables") and acknowledges support from the Spanish Ministry of Science, Innovation and Universities through grant ESP2017-89838, and the H2020 programme of the European Commission through grant 776247. The Euclid Consortium acknowledges the European Space Agency and a number of agencies and institutes that have supported the development of *Euclid*, in particular the Academy of Finland, the Agenzia Spaziale Italiana, the Belgian Science Policy, the Canadian Euclid Consortium, the French Centre National d'Etudes Spatiales, the Deutsches Zentrum für Luft- und Raumfahrt, the Danish Space Research Institute, the Fundação para a Ciência e a Tecnologia, the Ministerio de Ciencia e Innovación, the National Aeronautics and Space Administration, the National Astronomical Observatory of Japan, the Nederlandse Onderzoekschool Voor Astronomie, the Norwegian Space Agency, the Romanian Space Agency, the State Secretariat for Education, Research and Innovation (SERI) at the Swiss Space Office (SSO), and the United Kingdom Space Agency. A complete and detailed list is available on the *Euclid* web site (<http://www.euclid-ec.org>).

References

- Albrecht, A., Bernstein, G., Cahn, R., et al. 2006, *astro*
- Astropy Collaboration: Price-Whelan, A. M., Sipőcz, B. M., Günther, H. M., et al. 2018, *AJ*, 156, 123
- Astropy Collaboration: Robitaille, T. P., Tollerud, E. J., Greenfield, P., et al. 2013, *A&A*, 558, A33
- Barreira, A., Krause, E., & Schmidt, F. 2018a, *J. Cosmology Astropart. Phys.*, 10 (2018), 053
- Barreira, A., Krause, E., & Schmidt, F. 2018b, *J. Cosmology Astropart. Phys.*, 06 (2018), 015
- Barreira, A., Lazeyras, T., & Schmidt, F. 2021, *J. Cosmology Astropart. Phys.*, 08 (2021), 029
- Barreira, A., Nelson, D., Pillepich, A., et al. 2019, *MNRAS*, 488, 2079
- Barreira, A. & Schmidt, F. 2017, *J. Cosmology Astropart. Phys.*, 06 (2017), 053
- Bayer, A. E., Liu, J., Terasawa, R., et al. 2022, arXiv:2210.15647
- Bernardeau, F., Nishimichi, T., & Taruya, A. 2014, *MNRAS*, 445, 1526
- Bird, S., Viel, M., & Haehnelt, M. G. 2012, *MNRAS*, 420, 2551
- Blas, D., Lesgourgues, J., & Tram, T. 2011, *J. Cosmology Astropart. Phys.*, 07 (2011), 034
- Chevallier, M. & Polarski, D. 2001, *Int. J. Mod. Phys. D*, 10, 213
- Chisari, N. E., Alonso, D., Krause, E., et al. 2019, *ApJS*, 242, 2
- Cragg, C., Duncan, C. A. J., Miller, L., & Alonso, D. 2023, *MNRAS*, 518, 4909
- Crocce, M., Ross, A. J., Sevilla-Noarbe, I., et al. 2019, *MNRAS*, 482, 2807
- De Vicente, J., Sánchez, E., & Sevilla-Noarbe, I. 2016, *MNRAS*, 459, 3078
- Digman, M. C., McEwen, J. E., & Hirata, C. M. 2019, *J. Cosmology Astropart. Phys.*, 10 (2019), 004
- Esteban, I., Gonzalez-Garcia, M. C., Maltoni, M., Schwetz, T., & Zhou, A. 2020, *JHEP*, 09, 178
- Euclid Collaboration: Blanchard, A., Camera, S., Carbone, C., et al. 2020, *A&A*, 642, A191
- Euclid Collaboration: Casas, S. et al. 2023 [arXiv:2306.11053]
- Euclid Collaboration: Martinet, N., Schrabback, T., Hoekstra, H., et al. 2019, *A&A*, 627, A59
- Euclid Collaboration: Pocino, A., Tutusaus, I., Castander, F. J., et al. 2021, *A&A*, 655, A44
- Gouyou Beauchamps, S., Lacasa, F., Tutusaus, I., et al. 2022, *A&A*, 659, A128
- Hamilton, A. J. S., Rimes, C. D., & Scoccimarro, R. 2006, *MNRAS*, 371, 1188
- Harris, C. R., Millman, K. J., van der Walt, S. J., et al. 2020, *Nature*, 585, 357
- Hoyle, B., Gruen, D., Bernstein, G. M., et al. 2018, *MNRAS*, 478, 592
- Hu, W. & Kravtsov, A. V. 2003, *ApJ*, 584, 702
- Hunter, J. D. 2007, *Computing in Science and Engineering*, 9, 90
- Ivezić, Ž., Kahn, S. M., Tyson, J. A., et al. 2019, *ApJ*, 873, 111
- Jennings, E., Zuntz, J., Paterno, M., et al. 2016, in *Python in Astronomy 2016*, ed. T. Jenness, T. Robitaille, E. Tollerud, S. Mumford, & K. Cruz, 14
- Joachimi, B., Cacciato, M., Kitching, T. D., et al. 2015, *Space Sci. Rev.*, 193, 1
- Kaiser, N. 1998, *ApJ*, 498, 26
- Kilbinger, M., Heymans, C., Asgari, M., et al. 2017, *MNRAS*, 472, 2126
- Kitching, T. D., Alsing, J., Heavens, A. F., et al. 2017, *MNRAS*, 469, 2737
- Krause, E. & Eifler, T. 2017, *MNRAS*, 470, 2100
- Krause, E., Fang, X., Pandey, S., et al. 2021, arXiv:2105.13548
- Lacasa, F. 2020, *A&A*, 634, A74
- Lacasa, F., Aubert, M., Baratta, P., et al. 2023, *A&A*, 671, A115
- Lacasa, F. & Grain, J. 2019, *A&A*, 624, A61
- Lacasa, F., Lima, M., & Agüena, M. 2018, *A&A*, 611, A83
- Lacasa, F. & Rosenfeld, R. 2016, *J. Cosmology Astropart. Phys.*, 08 (2016), 005
- Lam, S. K., Pitrou, A., & Seibert, S. 2015, in *Proc. Second Workshop on the LLVM Compiler Infrastructure in HPC*, 1–6
- Laureijs, R., Amiaux, J., Arduini, S., et al. 2011, arXiv:1110.3193
- Lazeyras, T., Wagner, C., Baldauf, T., & Schmidt, F. 2016, *J. Cosmology Astropart. Phys.*, 02 (2016), 018
- Lewis, A., Challinor, A., & Lasenby, A. 2000, *ApJ*, 538, 473
- Li, Y., Hu, W., & Takada, M. 2014, *Phys. Rev. D*, 89, 083519
- Li, Y., Hu, W., & Takada, M. 2016, *Phys. Rev. D*, 93, 063507
- Limber, D. N. 1953, *ApJ*, 117, 134
- Linder, E. V. 2005, *Phys. Rev. D*, 72, 043529
- Linke, L., Burger, P. A., Heydenreich, S., Porth, L., & Schneider, P. 2023, arXiv e-prints, arXiv:2302.12277
- Pandey, S., Krause, E., DeRose, J., et al. 2022, *Phys. Rev. D*, 106, 043520
- Perlmutter, S., Aldering, G., Goldhaber, G., et al. 1999, *ApJ*, 517, 565
- Potter, D., Stadel, J., & Teysier, R. 2017, *Computational Astrophysics and Cosmology*, 4, 2
- Riess, A. G., Filippenko, A. V., Challis, P., et al. 1998, *AJ*, 116, 1009
- Rimes, C. D. & Hamilton, A. J. S. 2006, *MNRAS*, 371, 1205
- Rizzato, M., Benabed, K., Bernardeau, F., & Lacasa, F. 2019, *MNRAS*, 490, 4688
- Spergel, D., Gehrels, N., Baltay, C., et al. 2015, arXiv:1503.03757
- Takada, M. & Hu, W. 2013, *Phys. Rev. D*, 87, 123504
- Takahashi, R., Sato, M., Nishimichi, T., Taruya, A., & Oguri, M. 2012, *ApJ*, 761, 152
- Taylor, P. L., Kitching, T. D., McEwen, J. D., & Tram, T. 2018, *Physical Review D*, 98, 023522
- Tegmark, M., Taylor, A. N., & Heavens, A. F. 1997, *ApJ*, 480, 22
- Tinker, J. L., Robertson, B. E., Kravtsov, A. V., et al. 2010, *ApJ*, 724, 878
- Unruh, S., Schneider, P., Hilbert, S., et al. 2020, *A&A*, 638, A96
- Upham, R. E., Brown, M. L., Whittaker, L., et al. 2022, *A&A*, 660, A114
- Virtanen, P., Gommers, R., Oliphant, T. E., et al. 2020, *Nature Methods*, 17, 261
- Voivodic, R. & Barreira, A. 2021, *J. Cosmology Astropart. Phys.*, 05 (2021), 069
- Wadekar, D., Ivanov, M. M., & Scoccimarro, R. 2020, *Phys. Rev. D*, 102, 123521
- Wagner, C., Schmidt, F., Chiang, C. T., & Komatsu, E. 2015a, *MNRAS*, 448, L11
- Wagner, C., Schmidt, F., Chiang, C.-T., & Komatsu, E. 2015b, *J. Cosmology Astropart. Phys.*, 08 (2015), 042
- White, M., Blanton, M., Bolton, A., et al. 2011, *ApJ*, 728, 126
- Yao, J., Shan, H., Li, R., et al. 2023, arXiv e-prints, arXiv:2304.04489
- Zennaro, M., Angulo, R. E., Contreras, S., Pellejero-Ibáñez, M., & Maion, F. 2022, *MNRAS*, 514, 5443

¹ Dipartimento di Fisica, Sapienza Università di Roma, Piazzale Aldo Moro 2, 00185 Roma, Italy

² INAF-Osservatorio Astronomico di Roma, Via Frascati 33, 00078 Monteporzio Catone, Italy

³ INFN-Sezione di Roma, Piazzale Aldo Moro, 2 - c/o Dipartimento di Fisica, Edificio G. Marconi, 00185 Roma, Italy

⁴ Aix-Marseille Université, CNRS/IN2P3, CPPM, Marseille, France

⁵ Institut d'Estudis Espacials de Catalunya (IEEC), Carrer Gran Capità 2-4, 08034 Barcelona, Spain

⁶ Institut de Ciències de l'Espai (IEEC-CSIC), Campus UAB, Carrer de Can Magrans, s/n Cerdanyola del Vallès, 08193 Barcelona, Spain

⁷ Dipartimento di Fisica, Università degli Studi di Torino, Via P. Giuria 1, 10125 Torino, Italy

⁸ INFN-Sezione di Torino, Via P. Giuria 1, 10125 Torino, Italy

⁹ INAF-Osservatorio Astrofisico di Torino, Via Osservatorio 20, 10025 Pino Torinese (TO), Italy

¹⁰ Institut de Recherche en Astrophysique et Planétologie (IRAP), Université de Toulouse, CNRS, UPS, CNES, 14 Av. Edouard Belin, 31400 Toulouse, France

¹¹ Université de Genève, Département de Physique Théorique and Centre for Astroparticle Physics, 24 quai Ernest-Ansermet, CH-1211 Genève 4, Switzerland

¹² Institute of Space Sciences (ICE, CSIC), Campus UAB, Carrer de Can Magrans, s/n, 08193 Barcelona, Spain

¹³ Université Paris-Saclay, CNRS, Institut d'astrophysique spatiale, 91405, Orsay, France

¹⁴ Excellence Cluster ORIGINS, Boltzmannstrasse e 2, 85748 Garching, Germany

¹⁵ Ludwig-Maximilians-University, Schellingstrasse 4, 80799 Munich,

Germany

- ¹⁶ Department of Physics and Trottier Space Institute, McGill University, 3600 University Street, Montreal, QC H3A 2T8, Canada
- ¹⁷ University of Lyon, Univ Claude Bernard Lyon 1, CNRS/IN2P3, IP2I Lyon, UMR 5822, 69622 Villeurbanne, France
- ¹⁸ Université Clermont Auvergne, CNRS/IN2P3, LPC, F-63000 Clermont-Ferrand, France
- ¹⁹ Jodrell Bank Centre for Astrophysics, Department of Physics and Astronomy, University of Manchester, Oxford Road, Manchester M13 9PL, UK
- ²⁰ INAF-IASF Milano, Via Alfonso Corti 12, 20133 Milano, Italy
- ²¹ Institute for Theoretical Particle Physics and Cosmology (TTK), RWTH Aachen University, 52056 Aachen, Germany
- ²² Université Paris-Saclay, CNRS/IN2P3, IJCLab, 91405 Orsay, France
- ²³ Centre National d'Etudes Spatiales – Centre spatial de Toulouse, 18 avenue Edouard Belin, 31401 Toulouse Cedex 9, France
- ²⁴ Institut für Theoretische Physik, University of Heidelberg, Philosophenweg 16, 69120 Heidelberg, Germany
- ²⁵ Université St Joseph; Faculty of Sciences, Beirut, Lebanon
- ²⁶ Institute for Computational Science, University of Zurich, Winterthurerstrasse 190, 8057 Zurich, Switzerland
- ²⁷ Institute of Cosmology and Gravitation, University of Portsmouth, Portsmouth PO1 3FX, UK
- ²⁸ INAF-Osservatorio Astronomico di Brera, Via Brera 28, 20122 Milano, Italy
- ²⁹ INAF-Osservatorio di Astrofisica e Scienza dello Spazio di Bologna, Via Piero Gobetti 93/3, 40129 Bologna, Italy
- ³⁰ Dipartimento di Fisica e Astronomia, Università di Bologna, Via Gobetti 93/2, 40129 Bologna, Italy
- ³¹ INFN-Sezione di Bologna, Viale Berti Pichat 6/2, 40127 Bologna, Italy
- ³² Dipartimento di Fisica, Università di Genova, Via Dodecaneso 33, 16146, Genova, Italy
- ³³ INFN-Sezione di Genova, Via Dodecaneso 33, 16146, Genova, Italy
- ³⁴ Department of Physics "E. Pancini", University Federico II, Via Cinthia 6, 80126, Napoli, Italy
- ³⁵ INAF-Osservatorio Astronomico di Capodimonte, Via Moiarrello 16, 80131 Napoli, Italy
- ³⁶ Instituto de Astrofísica e Ciências do Espaço, Universidade do Porto, CAUP, Rua das Estrelas, PT4150-762 Porto, Portugal
- ³⁷ Institut de Física d'Altes Energies (IFAE), The Barcelona Institute of Science and Technology, Campus UAB, 08193 Bellaterra (Barcelona), Spain
- ³⁸ Port d'Informació Científica, Campus UAB, C. Albareda s/n, 08193 Bellaterra (Barcelona), Spain
- ³⁹ INFN section of Naples, Via Cinthia 6, 80126, Napoli, Italy
- ⁴⁰ Dipartimento di Fisica e Astronomia "Augusto Righi" - Alma Mater Studiorum Università di Bologna, Viale Berti Pichat 6/2, 40127 Bologna, Italy
- ⁴¹ Institut national de physique nucléaire et de physique des particules, 3 rue Michel-Ange, 75794 Paris Cédex 16, France
- ⁴² Institute for Astronomy, University of Edinburgh, Royal Observatory, Blackford Hill, Edinburgh EH9 3HJ, UK
- ⁴³ European Space Agency/ESRIN, Largo Galileo Galilei 1, 00044 Frascati, Roma, Italy
- ⁴⁴ ESAC/ESA, Camino Bajo del Castillo, s/n., Urb. Villafranca del Castillo, 28692 Villanueva de la Cañada, Madrid, Spain
- ⁴⁵ Institute of Physics, Laboratory of Astrophysics, Ecole Polytechnique Fédérale de Lausanne (EPFL), Observatoire de Sauvigny, 1290 Versoix, Switzerland
- ⁴⁶ UCB Lyon 1, CNRS/IN2P3, IUF, IP2I Lyon, 4 rue Enrico Fermi, 69622 Villeurbanne, France
- ⁴⁷ Mullard Space Science Laboratory, University College London, Holmbury St Mary, Dorking, Surrey RH5 6NT, UK
- ⁴⁸ Departamento de Física, Faculdade de Ciências, Universidade de Lisboa, Edifício C8, Campo Grande, PT1749-016 Lisboa, Portugal
- ⁴⁹ Instituto de Astrofísica e Ciências do Espaço, Faculdade de Ciências, Universidade de Lisboa, Campo Grande, 1749-016 Lisboa, Portugal
- ⁵⁰ Department of Astronomy, University of Geneva, ch. d'Ecogia 16, 1290 Versoix, Switzerland
- ⁵¹ INFN-Padova, Via Marzolo 8, 35131 Padova, Italy
- ⁵² INAF-Istituto di Astrofisica e Planetologia Spaziali, via del Fosso del Cavaliere, 100, 00100 Roma, Italy
- ⁵³ Université Paris-Saclay, Université Paris Cité, CEA, CNRS, AIM, 91191, Gif-sur-Yvette, France
- ⁵⁴ INAF-Osservatorio Astronomico di Trieste, Via G. B. Tiepolo 11, 34143 Trieste, Italy
- ⁵⁵ INAF-Osservatorio Astronomico di Padova, Via dell'Osservatorio 5, 35122 Padova, Italy
- ⁵⁶ Max Planck Institute for Extraterrestrial Physics, Giessenbachstr. 1, 85748 Garching, Germany
- ⁵⁷ University Observatory, Faculty of Physics, Ludwig-Maximilians-Universität, Scheinerstr. 1, 81679 Munich, Germany
- ⁵⁸ Dipartimento di Fisica "Aldo Pontremoli", Università degli Studi di Milano, Via Celoria 16, 20133 Milano, Italy
- ⁵⁹ INFN-Sezione di Milano, Via Celoria 16, 20133 Milano, Italy
- ⁶⁰ Institute of Theoretical Astrophysics, University of Oslo, P.O. Box 1029 Blindern, 0315 Oslo, Norway
- ⁶¹ Jet Propulsion Laboratory, California Institute of Technology, 4800 Oak Grove Drive, Pasadena, CA, 91109, USA
- ⁶² Department of Physics, Lancaster University, Lancaster, LA1 4YB, UK
- ⁶³ von Hoerner & Sulger GmbH, Schloßplatz 8, 68723 Schwetzingen, Germany
- ⁶⁴ Technical University of Denmark, Elektrovej 327, 2800 Kgs. Lyngby, Denmark
- ⁶⁵ Cosmic Dawn Center (DAWN), Denmark
- ⁶⁶ Institut d'Astrophysique de Paris, UMR 7095, CNRS, and Sorbonne Université, 98 bis boulevard Arago, 75014 Paris, France
- ⁶⁷ Max-Planck-Institut für Astronomie, Königstuhl 17, 69117 Heidelberg, Germany
- ⁶⁸ Department of Physics and Astronomy, University College London, Gower Street, London WC1E 6BT, UK
- ⁶⁹ Department of Physics and Helsinki Institute of Physics, Gustaf Hällströmin katu 2, 00014 University of Helsinki, Finland
- ⁷⁰ Department of Physics, P.O. Box 64, 00014 University of Helsinki, Finland
- ⁷¹ Helsinki Institute of Physics, Gustaf Hällströmin katu 2, University of Helsinki, Helsinki, Finland
- ⁷² NOVA optical infrared instrumentation group at ASTRON, Oude Hoogeveensedijk 4, 7991PD, Dwingeloo, The Netherlands
- ⁷³ Universität Bonn, Argelander-Institut für Astronomie, Auf dem Hügel 71, 53121 Bonn, Germany
- ⁷⁴ Aix-Marseille Université, CNRS, CNES, LAM, Marseille, France
- ⁷⁵ Dipartimento di Fisica e Astronomia "Augusto Righi" - Alma Mater Studiorum Università di Bologna, via Piero Gobetti 93/2, 40129 Bologna, Italy
- ⁷⁶ Department of Physics, Institute for Computational Cosmology, Durham University, South Road, DH1 3LE, UK
- ⁷⁷ Université Côte d'Azur, Observatoire de la Côte d'Azur, CNRS, Laboratoire Lagrange, Bd de l'Observatoire, CS 34229, 06304 Nice cedex 4, France
- ⁷⁸ Université Paris Cité, CNRS, Astroparticule et Cosmologie, 75013 Paris, France
- ⁷⁹ Institut d'Astrophysique de Paris, 98bis Boulevard Arago, 75014, Paris, France
- ⁸⁰ CEA Saclay, DFR/IRFU, Service d'Astrophysique, Bat. 709, 91191 Gif-sur-Yvette, France
- ⁸¹ European Space Agency/ESTEC, Keplerlaan 1, 2201 AZ Noordwijk, The Netherlands
- ⁸² Department of Physics and Astronomy, University of Aarhus, Ny Munkegade 120, DK-8000 Aarhus C, Denmark
- ⁸³ Université Paris-Saclay, Université Paris Cité, CEA, CNRS, Astrophysique, Instrumentation et Modélisation Paris-Saclay, 91191 Gif-sur-Yvette, France
- ⁸⁴ Space Science Data Center, Italian Space Agency, via del Politecnico snc, 00133 Roma, Italy
- ⁸⁵ Institute of Space Science, Str. Atomistilor, nr. 409 Măgurele, Ilfov, 077125, Romania
- ⁸⁶ Instituto de Astrofísica de Canarias, Calle Vía Láctea s/n, 38204, San

Cristóbal de La Laguna, Tenerife, Spain

⁸⁷ Departamento de Astrofísica, Universidad de La Laguna, 38206, La Laguna, Tenerife, Spain

⁸⁸ Dipartimento di Fisica e Astronomia "G. Galilei", Università di Padova, Via Marzolo 8, 35131 Padova, Italy

⁸⁹ Universitäts-Sternwarte München, Fakultät für Physik, Ludwig-Maximilians-Universität München, Scheinerstrasse 1, 81679 München, Germany

⁹⁰ Departamento de Física, FCFM, Universidad de Chile, Blanco Encalada 2008, Santiago, Chile

⁹¹ AIM, CEA, CNRS, Université Paris-Saclay, Université de Paris, 91191 Gif-sur-Yvette, France

⁹² Centro de Investigaciones Energéticas, Medioambientales y Tecnológicas (CIEMAT), Avenida Complutense 40, 28040 Madrid, Spain

⁹³ Instituto de Astrofísica e Ciências do Espaço, Faculdade de Ciências, Universidade de Lisboa, Tapada da Ajuda, 1349-018 Lisboa, Portugal

⁹⁴ Universidad Politécnica de Cartagena, Departamento de Electrónica y Tecnología de Computadoras, Plaza del Hospital 1, 30202 Cartagena, Spain

⁹⁵ Kapteyn Astronomical Institute, University of Groningen, PO Box 800, 9700 AV Groningen, The Netherlands

⁹⁶ INFN-Bologna, Via Irnerio 46, 40126 Bologna, Italy

⁹⁷ Infrared Processing and Analysis Center, California Institute of Technology, Pasadena, CA 91125, USA

⁹⁸ IFPU, Institute for Fundamental Physics of the Universe, via Beirut 2, 34151 Trieste, Italy

⁹⁹ Junia, EPA department, 41 Bd Vauban, 59800 Lille, France

¹⁰⁰ Instituto de Física Teórica UAM-CSIC, Campus de Cantoblanco, 28049 Madrid, Spain

¹⁰¹ CERCA/ISO, Department of Physics, Case Western Reserve University, 10900 Euclid Avenue, Cleveland, OH 44106, USA

¹⁰² Laboratoire de Physique de l'École Normale Supérieure, ENS, Université PSL, CNRS, Sorbonne Université, 75005 Paris, France

¹⁰³ Observatoire de Paris, Université PSL, Sorbonne Université, LERMA, 750 Paris, France

¹⁰⁴ Astrophysics Group, Blackett Laboratory, Imperial College London, London SW7 2AZ, UK

¹⁰⁵ Scuola Normale Superiore, Piazza dei Cavalieri 7, 56126 Pisa, Italy

¹⁰⁶ SISSA, International School for Advanced Studies, Via Bonomea 265, 34136 Trieste TS, Italy

¹⁰⁷ INFN, Sezione di Trieste, Via Valerio 2, 34127 Trieste TS, Italy

¹⁰⁸ Dipartimento di Fisica e Scienze della Terra, Università degli Studi di Ferrara, Via Giuseppe Saragat 1, 44122 Ferrara, Italy

¹⁰⁹ Istituto Nazionale di Fisica Nucleare, Sezione di Ferrara, Via Giuseppe Saragat 1, 44122 Ferrara, Italy

¹¹⁰ Institut de Physique Théorique, CEA, CNRS, Université Paris-Saclay 91191 Gif-sur-Yvette Cedex, France

¹¹¹ Dipartimento di Fisica - Sezione di Astronomia, Università di Trieste, Via Tiepolo 11, 34131 Trieste, Italy

¹¹² NASA Ames Research Center, Moffett Field, CA 94035, USA

¹¹³ Kavli Institute for Particle Astrophysics & Cosmology (KIPAC), Stanford University, Stanford, CA 94305, USA

¹¹⁴ INAF, Istituto di Radioastronomia, Via Piero Gobetti 101, 40129 Bologna, Italy

¹¹⁵ Institute Lorentz, Leiden University, PO Box 9506, Leiden 2300 RA, The Netherlands

¹¹⁶ Institute for Astronomy, University of Hawaii, 2680 Woodlawn Drive, Honolulu, HI 96822, USA

¹¹⁷ Department of Physics & Astronomy, University of California Irvine, Irvine CA 92697, USA

¹¹⁸ Departamento Física Aplicada, Universidad Politécnica de Cartagena, Campus Muralla del Mar, 30202 Cartagena, Murcia, Spain

¹¹⁹ Department of Astronomy & Physics and Institute for Computational Astrophysics, Saint Mary's University, 923 Robie Street, Halifax, Nova Scotia, B3H 3C3, Canada

¹²⁰ Dipartimento di Fisica, Università degli studi di Genova, and INFN-Sezione di Genova, via Dodecaneso 33, 16146, Genova, Italy

¹²¹ Ruhr University Bochum, Faculty of Physics and Astronomy, Astronomical Institute (AIRUB), German Centre for Cosmological Lensing (GCCL), 44780 Bochum, Germany

¹²² Caltech/IPAC, 1200 E. California Blvd., Pasadena, CA 91125, USA

¹²³ Department of Physics and Astronomy, Vesilinnantie 5, 20014 University of Turku, Finland

¹²⁴ Serco for European Space Agency (ESA), Camino bajo del Castillo, s/n, Urbanización Villafranca del Castillo, Villanueva de la Cañada, 28692 Madrid, Spain

¹²⁵ Oskar Klein Centre for Cosmoparticle Physics, Department of Physics, Stockholm University, Stockholm, SE-106 91, Sweden

¹²⁶ Univ. Grenoble Alpes, CNRS, Grenoble INP, LPSC-IN2P3, 53, Avenue des Martyrs, 38000, Grenoble, France

¹²⁷ Centre de Calcul de l'IN2P3/CNRS, 21 avenue Pierre de Coubertin 69627 Villeurbanne Cedex, France

¹²⁸ Centro de Astrofísica da Universidade do Porto, Rua das Estrelas, 4150-762 Porto, Portugal

¹²⁹ Dipartimento di Fisica, Università di Roma Tor Vergata, Via della Ricerca Scientifica 1, Roma, Italy

¹³⁰ INFN, Sezione di Roma 2, Via della Ricerca Scientifica 1, Roma, Italy

¹³¹ Department of Mathematics and Physics E. De Giorgi, University of Salento, Via per Arnesano, CP-193, 73100, Lecce, Italy

¹³² INAF-Sezione di Lecce, c/o Dipartimento Matematica e Fisica, Via per Arnesano, 73100, Lecce, Italy

¹³³ INFN, Sezione di Lecce, Via per Arnesano, CP-193, 73100, Lecce, Italy

¹³⁴ Higgs Centre for Theoretical Physics, School of Physics and Astronomy, The University of Edinburgh, Edinburgh EH9 3FD, UK

¹³⁵ Department of Astrophysical Sciences, Peyton Hall, Princeton University, Princeton, NJ 08544, USA

¹³⁶ Niels Bohr Institute, University of Copenhagen, Jagtvej 128, 2200 Copenhagen, Denmark

Appendix A: Details of the code validation

In the following Appendix, we provide an overview of the steps undertaken to compare and validate the codes used in this work, and some of the lessons learnt in the process.

In order to compute and validate the results we adopt the scheme sketched in Fig. A.1, which highlights the dependency of each main element of the forecast computation on the others. In particular, we have that:

1. The 1σ constraints are obtained from the FM through Eq. (47), and the FM is built in turn from the (inverse) covariance matrix and the derivatives of the angular PS $C_{ij}^{AB}(\ell)$ as indicated in Eq. (43).
2. The Gaussian covariance depends on the $C_{ij}^{AB}(\ell)$ through Eq. (24) (and the noise PS, Eq. 25). The SSC also depends on the $C_{ij}^{AB}(\ell)$, with the added contribution of the $R_{ij}^{AB}(\ell)$ terms and the output of the PySSC module, the S_{ijkl} matrix – following Eq. (10).
3. The $C_{ij}^{AB}(\ell)$ are constructed by convolving the (nonlinear) matter PS with the lensing and galaxy weight functions, as in Eq. (1). The S_{ijkl} matrix also depends on the weight functions (see Eq. 11), which are in fact the main external input needed by PySSC, and on the *linear* matter PS through the $\sigma^2(z_1, z_2)$ term (Eq. 5). It is to be noted, however, that PySSC computes this PS internally, needing only the specification of a dictionary of cosmological parameters with which to call the Boltzmann solver CLASS through the Python wrapper *classy*. This means that we also have to make sure that the fiducial value of the parameters used to compute the PS of Eq. (1) are the same ones passed to PySSC (this time to compute the linear PS), in order to work with the same cosmology.

While to compute the constraints we follow the scheme from right to left, starting from the basic ingredients to arrive at the final result, the general trend of the validation is the opposite: we begin by comparing the final results, then work our way back whenever we find disagreement.

We then start the comparison from the σ_α . If a discrepancy larger than 10% is found, we check the quantities they depend on, which in this case are the covariance matrices (see Eq. 43). If these agree, we check the codes directly. If these disagree, we iterate the process by checking the subsequent element in the scheme (in this case the S_{ijkl} matrix and the $C_{ij}^{AB}(\ell)$), until agreement is found. Essentially, this means that the disagreement in the outputs of the codes at each step can either come from the inputs, or from the codes themselves. Once the cause of the discrepancy is found and fixed, the computation is repeated and the process can start again.

The pipelines under comparison are both written in the Python language. One of them requires as external inputs the weight functions, the angular PS $C_{ij}^{AB}(\ell)$ and their derivatives with respect to the cosmological parameters; whilst the other produces these through the use of CosmoSIS¹⁵ (Jennings et al. 2016), and hence needs no external inputs but the vectors of fiducial cosmological and nuisance parameters. For the reader wishing to repeat the validation, we list below some of the lessons learnt in the code comparison process.

- PySSC needs as input the WL and GCph kernels of Eqs. (18) and (21), as well as their argument, the redshift values. The

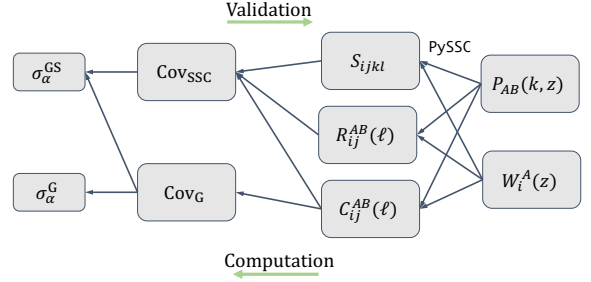


Fig. A.1. Some of the most important elements examined in the comparison. The arrows show the ordering followed to produce the parameters constraints, which is opposite to the one followed to validate the code. The derivatives of the PS with respect to the cosmological parameters, entering the final step of the computation, are not shown.

code then uses this redshift array to perform the necessary integrals in dV through Simpson’s rule. The user is responsible for sampling the kernels on a sufficiently fine z grid [$O(10^4)$ values have been found to be sufficient in the present case] to make sure these integrals are performed accurately.

- The latest version of PySSC accepts a `convention` parameter. This specifies whether the kernels are in the form used in LG19 (`convention = 0`) or the one prescribed in EC20 (`convention = 1`). The two differ by a $1/r^2(z)$ factor, as shown in Eq. (23). Passing the kernels in the EC20 form without changing the parameter’s value from 0 – the default – to 1 will obviously yield incorrect results.
- The ordering of the S_{ijkl} matrix’s elements depends on the ordering chosen when passing the input kernels to PySSC – whether $W_i^L(z)$ first and $W_i^G(z)$ second or vice versa. This must be kept in mind when implementing Eq. (10).
- The GCph constraints can show a discrepancy greater the 10% for the dark energy equation of state parameters w_0 and w_a even when the corresponding covariance is found to be in good agreement. This discrepancy is due to GCph being less numerically stable because of the lower constraining power compared to the other probes, and because the bias model considered has a strong degeneracy with σ_8 , making the numerical derivatives unstable (see e.g., [Euclid Collaboration: Casas et al. 2023](#)). Since this is a known issue, not coming from the SSC computation, and the covariance matrices and angular PS show good agreement, we choose to overcome the problem by using, for GCph, one code to compute both sets of parameter constraints (that is, we run one FM evaluation code with as input the covariance matrices from both groups).

Appendix B: High order bias from halo model

As described in Sect. 3.6.1, the higher-order bias $b_{(2)}(z)$ has been estimated using the halo model. In the following Appendix, we provide further details on the input quantities, and how we set the relevant parameters.

A key role is played by the halo mass function $\Phi_{MF}(M, z)$, which we model as

$$\Phi_{MF}(M, z) = \frac{\bar{\rho}_m}{M} f(\nu) \frac{d \ln \sigma^{-1}}{dM}, \quad (\text{B.1})$$

with M the halo mass, $\bar{\rho}_m$ the mean matter density, $\nu = \delta_c / \sigma(M, z)$, $\delta_c = 1.686$ the critical overdensity for collapse, and

¹⁵<https://bitbucket.org/joezuntz/cosmosis/wiki/Home>

$\sigma(M, z)$ the variance of linear perturbation smoothed with a top-hat filter of radius $R = [3M/(4\pi\bar{\rho}_m)]^{1/3}$. We follow [Tinker et al. \(2010\)](#), setting

$$f(v) = \mathcal{N}_{\text{MF}} \left[1 + (\beta_{\text{MF}} v)^{-2\phi_{\text{MF}}} \right] v^{2\eta_{\text{MF}}} \exp\left(-\gamma_{\text{MF}} v^2/2\right), \quad (\text{B.2})$$

where \mathcal{N}_{MF} is a normalisation constant, and the halo mass function fitting parameters β_{MF} , η_{MF} , γ_{MF} and ϕ_{MF} – not to be confused with $\Phi_{\text{MF}}(M, z)$ – scale with redshift as illustrated in Eqs. (9–13) of the above-mentioned paper.

The other quantity needed is the average number of galaxies hosted by a halo of mass M at redshift z . This is given by

$$\langle N|M \rangle(M) = N_{\text{cen}}(M) [1 + N_{\text{sat}}(M)] , \quad (\text{B.3})$$

where $N_{\text{cen}}(M, z)$ and $N_{\text{sat}}(M, z)$ account for the contributions of central and satellite galaxies, respectively. We model these terms as in [White et al. \(2011\)](#)

$$N_{\text{cen}}(M) = \frac{1}{2} \left\{ 1 + \text{erfc} \left[\frac{\ln(M/M_{\text{cut}})}{\sqrt{2}\sigma_c} \right] \right\} , \quad (\text{B.4})$$

$$N_{\text{sat}}(M) = \begin{cases} 0 & M < \kappa_s M_{\text{cut}} \\ \left(\frac{M - \kappa_s M_{\text{cut}}}{M_1} \right)^{\alpha_s} & M \geq \kappa_s M_{\text{cut}}, \end{cases} \quad (\text{B.5})$$

with fiducial parameter values

$$\{\log_{10}(M_{\text{cut}}/M_{\odot}), \log_{10}(M_1/M_{\odot}), \sigma_c, \kappa_s, \alpha_s\} = \{13.04, 14.05, 0.94, 0.93, 0.97\} , \quad (\text{B.6})$$

M_{\odot} being the mass of the Sun. These values give the best fit to the clustering of massive galaxies at $z \sim 0.5$ as measured from the first semester of BOSS data. It is, however, expected that they are redshift-dependent although the precise scaling with z also depends on the galaxy population used as a tracer. We, therefore, adjust them so that the predicted galaxy bias matches, at each given redshift, our measured values from the Flagship simulation. Since, for each z , we have a single observable quantity, we can not fit all parameters. On the contrary, we fix all of them but M_{cut} to their fiducial values and use Eq. (40) to compute the bias as a function of M_{cut} . We then solve with respect to M_{cut} repeating this procedure for each redshift bin. We then linearly interpolate these values to get M_{cut} as a function of z , and use it to compute $b_{(2)}(z)$. Although quite crude, we have verified that changing the HOD parameter to be adjusted (e.g., using σ_c or M_1) has a negligible impact on the predicted $R^{\text{gm}}(\ell)$ and $R^{\text{gg}}(\ell)$.

Appendix C: Multipole binning

We bin the ℓ space according to the following procedure: the ℓ_k values, where $k = 1, \dots, \mathcal{N}_{\ell}$, are the centers of $\mathcal{N}_{\ell} + 1$ logarithmically equispaced values, λ_k , which act as the edges of the \mathcal{N}_{ℓ} bins:

$$\ell_k = \text{dex} \left[(\lambda_k^- + \lambda_k^+) / 2 \right] , \quad (\text{C.1})$$

with $\text{dex}(x) = 10^x$, $(\lambda_k^-, \lambda_k^+) = (\lambda_k, \lambda_{k+1})$, and

$$\lambda_k = \lambda_{\text{min}}^{\text{XC}} + (k-1)(\lambda_{\text{max}}^{\text{XC}} - \lambda_{\text{min}}^{\text{XC}}) / \mathcal{N}_{\ell} , \quad (\text{C.2})$$

being

$$\{\lambda_{\text{min}}^{\text{XC}}, \lambda_{\text{max}}^{\text{XC}}\} = \{\log_{10}(\ell_{\text{min}}^{\text{XC}}), \log_{10}(\ell_{\text{max}}^{\text{XC}})\} . \quad (\text{C.3})$$

In order to compute the Gaussian covariance, we also need the width of the bin, which will simply be

$$\Delta\ell_k = \text{dex}(\lambda_{k+1}) - \text{dex}(\lambda_k) , \quad (\text{C.4})$$

so that $\Delta\ell_k$ is not the same for all bins, since the bins are logarithmically – and not linearly – equispaced.